



# TECHNICAL MEMORANDUM

X-286  
TO

EFFECTS OF WING PLAN-FORM GEOMETRY ON THE AERODYNAMIC  
CHARACTERISTICS OF A HYPERSONIC GLIDER AT MACH

NUMBERS UP TO 9.6

By Charles L. Ladson, Patrick J. Johnston,  
and Charles D. Trescot, Jr.

Langley Research Center  
Langley Field, Va.

(NASA-TM-X-286) EFFECTS OF WING PLAN  
FORM GEOMETRY ON THE AERODYNAMIC  
CHARACTERISTICS OF A HYPERSONIC GLIDER AT  
MACH NUMBERS UP TO 9.6 (NASA) 61 p

N73-73888

Unclas  
00/99 08308

NATIONAL AERONAUTICS AND SPACE ADMINISTRATION

WASHINGTON

May 1960

[REDACTED]  
NATIONAL AERONAUTICS AND SPACE ADMINISTRATION

## TECHNICAL MEMORANDUM X-286

EFFECTS OF WING PLAN-FORM GEOMETRY ON THE AERODYNAMIC  
CHARACTERISTICS OF A HYPERSONIC GLIDER AT MACH  
NUMBERS UP TO 9.6\*

By Charles L. Ladson, Patrick J. Johnston,  
and Charles D. Trescot, Jr.

## SUMMARY

An investigation has been conducted at the Langley Research Center on a winged, lifting hypersonic glider configuration to study the effects of wing crank and wing longitudinal location on the performance and static stability characteristics of such a vehicle throughout the Mach number range. Tests were conducted at Mach numbers of 0.92, 1.62, 2.91, 6.8, and 9.6 and are presented with previously published data at a velocity of 60 feet per second.

From an analysis of the data obtained during this investigation, it is noted that the rearward shifts of aerodynamic center and center of pressure which occur at transonic speeds were less for the configurations with wing and body apexes coincident. At a Mach number of 9.6, the aerodynamic center is slightly rearward of the location at subsonic speeds, whereas the center of pressure has moved forward of its subsonic location.

Moving the centroid of area rearward (and thus the center of pressure) by cranking the wing leading edge increased the longitudinal stability throughout the Mach number range for the configuration with the wing and body vertex coincident. However, with the wing moved rearward on the body, and with the centroid of area displaced forward slightly by cranking the leading edge, a loss of stability at Mach numbers above about 3 resulted.

The local flow conditions in the region of the fins had a strong influence upon the directional stability of the configurations. Whenever the body shock moved outboard of the tip fins as a result of either a reduction in Mach number or an increase in sideslip angle, the fin effectiveness was reduced and the stability of the vehicle was likewise reduced. Likewise, at hypersonic speeds the cranked-wing vehicle with the body shock wave inboard of the tip fins had more directional stability than the uncranked vehicle at an angle of attack of  $0^\circ$ , but the fall-off at the highest angles of attack was more severe for the cranked-wing vehicle.

---

[REDACTED]

[REDACTED]

## INTRODUCTION

Hypersonic boost glide configurations, which should be statically stable and controllable from hypersonic gliding speeds to subsonic landing speeds, could encounter serious stability and control problems due to a shift in the location of the aerodynamic center with Mach number. Since little information is available on the extent of the aerodynamic-center travel on a configuration throughout this large Mach number range, an investigation was undertaken at the Langley Research Center with a winged, lifting vehicle with various plan-form shapes. The variations in wing plan-form geometry included two different longitudinal locations of the delta-wing body intersection and the use of leading-edge crank. It was desirable to determine whether either the wing location or the leading-edge crank is an effective means of reducing the aerodynamic-center travel with Mach number; thus, the longitudinal stability and control problems associated with large aerodynamic-center shifts are reduced. Since the configuration also incorporated vertical tip fins mounted above the wing plane to provide directional stability, it was desirable to study their effectiveness at the supersonic and hypersonic speeds and to determine what, if any, the effect of the wing plan form was on their effectiveness.


L  
7  
4  
2

Longitudinal tests were conducted on the configurations in the Langley transonic blowdown tunnel at a Mach number of 0.92, the Langley 9-inch tunnel at Mach numbers of 1.62 and 2.91, and the Langley 11-inch hypersonic tunnel at Mach numbers of 6.8 and 9.6 and limited tests at a Mach number of 17.8 in helium. Some previously published data (ref. 1) on these configurations obtained in the Langley free-flight tunnel at a velocity of 60 feet per second (Mach number of 0.06) are also included for comparison.

## SYMBOLS

|           |  |
|-----------|--|
| $b$       | span   |
| $\bar{c}$ | mean aerodynamic chord   |
| $C_D$     | drag coefficient   |
| $C_{D0}$  | drag coefficient at zero lift  |
| $C_l$     | rolling-moment coefficient about body center line,<br><u>Rolling moment</u><br>$qSb$ |

|                |   |
|----------------|---|
| $C_L$          | lift coefficient, $\frac{\text{Lift}}{qS}$  |
| $C_m$          | pitching-moment coefficient about moment center at 0.64l,<br>$\frac{\text{Pitching moment}}{qS\bar{c}}$   |
| $C_n$          | yawing-moment coefficient about moment center at 0.64l,<br>$\frac{\text{Yawing moment}}{qSb}$   |
| $C_N$          | normal-force coefficient, $\frac{\text{Normal force}}{qS}$  |
| $C_Y$          | side-force coefficient, $\frac{\text{Side force}}{qS}$  |
| $C_{L_\alpha}$ | lift-curve slope, $\left(\frac{\partial C_L}{\partial \alpha}\right)_{\alpha=0}$  |
| $C_{l_\beta}$  | rate of change of rolling-moment coefficient with angle of<br>sideslip at zero sideslip angle, $\left(\frac{\partial C_l}{\partial \beta}\right)_{\beta=0}$ |
| $C_{n_\beta}$  | rate of change of yawing-moment coefficient with angle of<br>sideslip at zero sideslip angle, $\left(\frac{\partial C_n}{\partial \beta}\right)_{\beta=0}$  |
| $C_{Y_\beta}$  | rate of change of side-force coefficient with angle of<br>sideslip at zero sideslip angle, $\left(\frac{\partial C_Y}{\partial \beta}\right)_{\beta=0}$     |
| $i_n$          | nose-incidence angle, deg   |
| $l$            | body length   |
| $L/D$          | lift-drag ratio   |
| $(L/D)_{\max}$ | maximum lift-drag ratio   |
| $M$            | Mach number   |




|          |   |
|----------|---|
| q        | dynamic pressure                            |
| R        | Reynolds number based on body length        |
| r        | radius                                      |
| S        | plan-form area, sq in.                      |
| $x_{ac}$ | longitudinal location of aerodynamic center |
| $x_{cp}$ | longitudinal location of center of pressure |
| $\alpha$ | angle of attack, deg                        |
| $\beta$  | angle of sideslip, deg                      |

## MODELS AND DESIGNATIONS

Three-view drawings showing the dimensions of the models tested as well as tables listing the calculated wing plan-form areas, spans, and mean aerodynamic chords are presented in figure 1. The various models are designated by letter symbols and subscripts and are identified as follows:

|       |   |
|-------|---|
| $B_1$ | body, shown in figure 1(a) and the same for all models tested                                       |
| $W_1$ | 74.25° swept clipped-tip delta wing shown in figure 1(a)  |
| $W_2$ | 60° swept clipped-tip delta wing shown in figure 1(a)   |
| $W_3$ | 68°, 60° cranked leading-edge clipped-tip delta wing shown in figure 1(a)                           |
| $W_4$ | 76°, 60° cranked leading-edge clipped-tip delta wing shown in figure 1(a).                          |
| $V_1$ | 40° swept leading-edge upper vertical tail shown in figure 1(a)                                     |
| $V_3$ | $V_1$ modified by increasing chord and adding 76° swept leading-edge lower fin shown in figure 1(b) |
| $F_2$ | rearward flap extension of wing plan form shown in figure 1(b)                                      |



The models were constructed of stainless steel, had flat-wing lower surfaces with  $5^\circ$  nose deflection to provide trim at angles of attack near  $(L/D)_{\max}$ , and incorporated  $5^\circ$  wedge-section vertical-tip fins toed in  $5^\circ$  to provide directional stability. The model nose was blunted to a radius of 0.09 inch and all leading edges had a radius of 0.024 inch normal to the leading edge. Model  $B_1W_4V_1$  was also tested with the nose incidence increased from  $5^\circ$  to  $7.5^\circ$  by cutting the model 2.70 inches behind the nose and bending the section of the model forward of this station upward until the incidence of the forward section was  $7.5^\circ$ .

Because of machining errors, the  $V_1$  tails used on the  $W_4$  wing had a slightly longer chord than called for. This error resulted in a 9.8 percent larger area for this fin on  $W_4$  than on the other three wings.

Model photographs are presented in figure 2.

#### APPARATUS, TESTS, AND PROCEDURE

Data contained in this report were obtained at  $M = 0.92$  in the Langley transonic blowdown tunnel,  $M = 1.62$  and  $2.91$  in the Langley 9-inch tunnel, and  $M = 6.8$  and  $9.6$  in air and  $17.8$  in helium in the Langley 11-inch hypersonic tunnel.

In the Langley transonic blowdown tunnel, which has an octagonal slotted throat test section measuring 26 inches between flats, the models were mounted on an internal 5-component electrical strain-gage balance (no axial-force measurements). The longitudinal tests were made at a tunnel stagnation pressure of 25 pounds per square inch absolute, which corresponds to a Reynolds number of  $4.1 \times 10^6$  based on model length.

For the tests at supersonic speeds in the Langley 9-inch tunnel, the models were mounted on a three-component mechanical external balance. Tests were made at a Reynolds number of about  $2.0 \times 10^6$  based on model length.

Some longitudinal tests in the Langley 11-inch hypersonic tunnel were made by using an external 3-component electrical strain-gage balance whereas other longitudinal and the directional and lateral tests were made on an internal 6-component strain-gage balance. The Reynolds numbers based on model length for the external balance were  $2.0 \times 10^6$  at  $M = 6.8$  and  $2.9 \times 10^6$  at  $M = 17.8$  and for the internal balance were  $1.3 \times 10^6$  at  $M = 6.8$  and  $0.6 \times 10^6$  at  $M = 9.6$ . In both the Langley

9-inch and 11-inch tunnels the angles of attack of the models were measured optically by use of a light beam reflected from the model onto a calibrated scale. This method gave the true angles of attack of the model including the deflection of the balance and sting under load. True angles of attack of the models were also obtained in the transonic blow-down tunnel by calibration of the balance deflection under known loads. Base pressures were measured in both the 9-inch and 11-inch tunnels and the data presented have been adjusted to a condition where base pressure is equal to free-stream static pressure.

## PRESENTATION OF RESULTS

Typical schlieren flow photographs of the models are presented in figure 3 at Mach numbers of 1.62, 2.91, 6.8, and 9.6. In figure 3(c) it can be seen that the body shock wave crosses the wing inboard of the vertical-tip fins for models  $B_1W_2V_1$ ,  $B_1W_3V_1$ , and  $B_1W_4V_1$  at  $\beta = 0^\circ$ . As the sideslip angle is increased to about  $5^\circ$ , the body shock crosses the downwind fin and at higher sideslip angles lies well outboard of the fin. The effects of this shock-fin interaction on directional stability are discussed later in the paper.

The basic longitudinal data obtained on the six configurations tested are presented in figures 4 to 7 as a function of angle of attack for the various Mach numbers. Lift coefficient is presented in figure 4, drag coefficient in figure 5, pitching-moment coefficient in figure 6, and lift-drag ratio in figure 7. Since no axial-force data were obtained during the  $M = 0.92$  tests,  $C_N \cos \alpha$  is presented in figure 4, and no  $C_D$  curve is presented in figure 5 for this Mach number. Data on configurations  $B_1W_1V_3F_2$  and  $B_1W_4V_3F_2$  are shown only for the supersonic and hypersonic Mach numbers. Additional data on models  $B_1W_1V_3F_2$  and  $B_1W_4V_3F_2$  at transonic Mach numbers are presented in reference 2. Analysis of this basic data is presented in figures 8 to 14. Basic directional stability characteristics of the configurations at  $M = 2.91$  are presented in figures 15 and 16 for angles of attack of  $0^\circ$  and  $10^\circ$ . No lateral data were obtained during the  $M = 2.91$  tests. Analysis of the directional and lateral data through the Mach number range is presented in figures 17 to 22.

## DISCUSSION

## Lift and Performance

Angle-of-attack effects.- In figure 4 the low subsonic lift curve is noted to break at an angle of attack of about  $20^\circ$ . This break is more clearly shown in figure 8 which presents the subsonic lift curves taken from reference 1 for the four basic models at angles of attack up to  $90^\circ$ . From this figure it is seen that all four configurations show a loss in lift-curve slope which is not regained until a much higher angle of attack. The cranked-wing configuration  $B_1W_4V_1$  has the most severe break and a loss of lift results which is not regained until the angle of attack has been increased about  $15^\circ$ . This loss of lift is probably caused by the large body interfering with the wing vortex flow and disrupting the vortex. Unpublished data indicate that this break in the lift curve can be eliminated by reducing the body size or by moving the body back on the wing. When the speed was increased to the hypersonic range, as expected, a noticeable increase in  $C_{L_\alpha}$  with  $\alpha$  occurred. (See fig. 4.)

Mach number effects.- The variation in the lift-curve slope at  $\alpha = 0^\circ$  of the configurations with Mach number is presented in figure 9. Little effect of wing crank or wing longitudinal position is noted at Mach numbers of 2.91 and above. However, at the transonic and low supersonic Mach numbers, the effects of aspect ratio on lift-curve slope become evident. Configurations  $B_1W_2V_1$  and  $B_1W_3V_1$ , which have aspect ratios of about 1.5 have a higher  $C_{L_\alpha}$  at Mach numbers of 0.92 and 1.62 than do models  $B_1W_1V_1$  and  $B_1W_4V_1$  which have aspect ratios of about 1.0 and 1.2, respectively. The trends in  $C_{L_\alpha}$  with Mach number agree well with inviscid flat-plate theory at the hypersonic speeds. The test point at  $M = 17.8$  is higher than the theory because of increased boundary-layer displacement effects at this Mach number and to a lesser extent as a result of using helium for the test fluid. The measurements using configurations with the higher wing sweep ( $B_1W_1V_1$  and  $B_1W_4V_1$ ) agree well with the theoretical  $C_{L_\alpha}$  for a  $75^\circ$  swept delta wing at supersonic Mach numbers. The measured values of  $C_{L_\alpha}$  on configurations  $B_1W_2V_1$  and  $B_1W_3V_1$  are below the theory for a  $60^\circ$  swept wing since the model plan form is not a true  $60^\circ$  delta but a cranked  $82.5^\circ$ ,  $60^\circ$  wing because of the flat bottom of the body which extends ahead of the actual wing.



Mach number effects on  $(L/D)_{\max}$ , presented in figure 10, followed the trends in  $C_{L\alpha}$  (reduction with increase in  $M$ ) and at low supersonic speeds, in general, the configurations with the highest  $C_{L\alpha}$  have the highest  $(L/D)_{\max}$ . This is to be expected since

$$(L/D)_{\max} = \frac{1}{2} \left( \frac{C_{L\alpha}}{C_{D0}} \right)^{1/2} \quad \text{if it is assumed that } C_L = C_{L\alpha} \alpha \text{ and}$$

$C_D = C_{D0} + C_{L\alpha} \alpha^2$ . At Mach numbers of 2.91 and above, all configurations have about the same  $(L/D)_{\max}$ . The higher value of  $(L/D)_{\max}$  at  $M = 17.8$  resulted from the lower skin friction at the higher Reynolds number of the test.

Fin and nose-incidence effects.— The effects on the performance characteristics of removing the vertical fin or of increasing the nose incidence are presented in figure 11 for model  $B_1W_4V_1$  at  $M = 6.8$ . As seen in figure 11(a), addition of the vertical fin  $V_1$  to the basic wing-body  $B_1W_4$  increases the drag coefficient as expected but also decreases the lift coefficient throughout the angle-of-attack range. This loss in lift is attributed to the high pressure interference region created on the wing upper surface between the fin and the fin shock wave. This fin shock wave may be seen behind the wing in the schlieren flow photographs presented in figure 3(c). Addition of the vertical fins resulted in about 20-percent decrease in the  $(L/D)_{\max}$  at this Mach number with little effect at higher angles of attack where the fin drag is reduced. Increasing the nose incidence from  $5^\circ$  to  $7.5^\circ$ , as shown in figure 11(b), increased the lift coefficient due to increasing the angle of attack of the nose and decreased the drag coefficient at low angles of attack. Although nose tilt increases the drag of the nose, the reduction in body axial force due to body shielding by the increased nose tilt more than cancelled it and a net reduction in drag resulted. Although increasing the nose incidence increased the  $L/D$  at low angles of attack as the angle of attack is increased, the differences in  $C_L$  and  $C_D$  diminish so that no effect is noted on  $(L/D)_{\max}$ . Similar results have been obtained in previous tests at  $M = 6.8$  and are presented in references 3 and 4.

### Longitudinal Stability

Longitudinal stability characteristics of the configurations tested are presented in figure 12 as plots of  $C_m$  against  $C_N$ . With

the forward location of the wing-body intersection (configurations  $B_1W_1V_1$  and  $B_1W_4V_1$ ), cranking the wing leading edge moved the centroid of area rearward 0.0191 and increased the longitudinal stability for all Mach numbers tested. However, for configurations  $B_1W_2V_1$  and  $B_1W_3V_1$ , cranking the wing leading edge moved the centroid of area forward 0.0041 and had no appreciable effect at Mach numbers of 2.91 and below, whereas at the higher speeds a loss in stability resulted.

Mach number effects.— The effects of Mach numbers on center-of-pressure location ( $C_m/C_N$ ) and aerodynamic-center location ( $\partial C_m/C_N$ ) (relative to the 0.641 body station) are shown in figure 13(a) for all configurations at an angle of attack of  $10^\circ$ . Both the aerodynamic center and the center of pressure move rearward at transonic speeds, the most rearward location probably occurring between  $M = 1$  and  $M = 2$ . At Mach numbers above 1.62 the aerodynamic center and center of pressure move forward and at the highest speed tested the aerodynamic center is slightly rearward of its subsonic location whereas the center of pressure is generally slightly forward. Although the different models have different levels of stability, all show the same general trends in the aerodynamic-center and center-of-pressure locations with Mach number.

Figure 13(b) presents the aerodynamic-center and center-of-pressure locations at  $\alpha = 10^\circ$  for a moment center located at the centroid of plan-form area for each configuration rather than at the 0.641 body station as in figure 13(a). The same trends with Mach number are again noted and it is also seen that the aerodynamic-center and center-of-pressure locations with respect to the centroid of plan-form area are a function of Mach number. At  $M = 9.6$ , the aerodynamic center is within about 0.061 of the centroid of area and, although not shown, moves closer as the angle of attack is increased. Although a comparison of total aerodynamic-center and center-of-pressure travel throughout the Mach number range cannot be made because of the limited data in the transonic range, it appears that the configurations with the wing and body vertex coincident ( $B_1W_1V_1$  and  $B_1W_4V_1$ ) would have the least travel. Since the center of gravity of a vehicle must be far enough forward to provide stability at subsonic and hypersonic speeds, the rearward travel of the center-of-pressure location at transonic speeds should be kept at a minimum to reduce the force needed to trim.

Fin and nose-incidence effects.— The decrease in lift coefficient at  $M = 6.8$  due to adding the vertical fin  $V_1$ , previously mentioned under the section "Lift and Performance," is also reflected in a positive increment in pitching moment as seen in figure 14(a) as a result of the fin-induced high-pressure interference region on the wing upper surface. Nose incidence was shown in reference 5 to be an effective means of trim at angles of attack for maximum  $L/D$ . Increasing the nose

incidence from  $5^\circ$  to  $7.5^\circ$  increased the positive pitching moment throughout the range tested (fig. 14(b)). The loss in stability is due to the rate of change of loading on the nose being greater than that on the remainder of the vehicle in this angle-of-attack range. At a  $C_N$  of about 0.40, the increment in  $C_m$  between the  $5^\circ$  and  $7.5^\circ$  nose is about twice that obtained at  $C_N = 0$ . Thus, while the  $i_n = 5^\circ$  configuration would trim at  $\alpha = 24^\circ$  ( $C_N = 0.41$ ), the  $i_n = 7.5^\circ$  configuration would trim at a much higher angle of attack.

### Lateral and Directional Stability

Directional and lateral stability characteristics of models  $B_1W_1$  and  $B_1W_4$  with the various vertical tails and flaps are presented at  $M = 6.8$  in figure 17 and  $M = 9.6$  in figure 18. With vertical tails  $V_1$ , the cranked-wing configuration  $B_1W_4V_1$  has a higher  $C_{n\beta}$  than the uncranked configuration at  $\alpha = 0^\circ$  but falls off to zero at a slightly lower angle of attack. With vertical tails  $V_3$ , little difference is noted between the cranked- and uncranked-wing configurations at  $M = 6.8$ . Although the vertical fins  $V_1$  on the cranked-wing model  $B_1W_4$  had about 10-percent larger plan-form area than the fins on the other models, this increase in area does not account for all the higher fin effectiveness of the cranked-wing model  $B_1W_4V_1$  at  $\alpha = 0^\circ$ .

Both models with and without vertical tails  $V_1$  exhibit a positive  $C_{l\beta}$  (negative dihedral effect) at angles of attack up to  $8^\circ$  at Mach numbers of 6.8 and 9.6. (See figs. 17 and 18.) Above this angle, a positive dihedral effect is noted. These same trends were also noted in tests of a high  $L/D$  flat-bottomed glider presented in reference 3. It is believed that this negative dihedral effect at low angles of attack is a result of body interference on the wing upper surface although no component breakdown or pressure-distribution studies have been made to support this belief. Adding the ventral fin (vertical tail  $V_3$ ) resulted in the negative dihedral effect being extended to the highest angle of attack tested as would be expected.

Mach number effects. - Figure 19 summarizes the Mach number effects on  $C_{n\beta}$  and  $C_{y\beta}$  at an angle of attack of  $10^\circ$ . The vehicle with the uncranked-wing plan form  $B_1W_1V_1$  shows a continuous decrease in both  $C_{n\beta}$  and  $C_{y\beta}$  with Mach number increase as would be expected from pure

Mach number effects. The schlieren flow photographs in figures 3(b) and 3(c) at Mach numbers of 2.91 and 6.8 show no changes other than angular in the general shock pattern for this configuration. The vehicle with the cranked-wing plan form  $B_1W_4V_1$ , however, has a lower  $C_{n\beta}$  at  $M = 2.91$  than the uncranked vehicle, probably because of the lower angle of the fin relative to the local flow behind the shock generated by the leading-edge crank. An increase in  $C_{n\beta}$  occurs between  $M = 2.91$  and  $M = 6.8$  on this cranked-wing vehicle, although it does show a decrease between  $M = 6.8$  and  $M = 9.6$  as did the uncranked vehicle. An explanation of these trends is possible from an examination of the schlieren flow photographs in figures 3(b) and 3(c) which show an appreciable change in the extent of the body flow field on the tip fins for the cranked-wing configurations between  $M = 2.91$  and  $M = 6.8$ . At  $M = 6.8$  the body shock is swept inboard of the vertical-tip fins at  $\beta = 0^\circ$  and the angle of the fin relative to the flow was increased. Also, the shock moves outboard as  $\beta$  is increased and thus impinges on the downwind fin at low sideslip angles. This shock impingement on the downwind fin increased the pressure on the inner surface and evidently cancels the expected destabilizing input of this fin and results in a higher total  $C_{n\beta}$  at  $M = 6.8$  than is noted at  $M = 2.91$ . Since no significant changes in the body flow field would be expected to occur between  $M = 6.8$  and  $M = 9.6$ , the  $C_{n\beta}$  loss with increase in Mach number shown in figure 19 is expected. The increment in  $C_{n\beta}$  and  $C_{y\beta}$  due to adding the vertical fins presented in figure 20 show the same trends as the total  $C_{n\beta}$  and  $C_{y\beta}$  of the vehicle.

Effects of nose incidence and sideslip angle.— The effect of increasing the nose incidence of model  $B_1W_4V_1$  from  $5^\circ$  to  $7.5^\circ$  at a Mach number of 6.8 is presented in figure 21. At sideslip angles above about  $5^\circ$ , the increased nose incidence decreased the directional stability, probably because of an alteration of the local flow over the tip fins.

The lateral and directional characteristics of model  $B_1W_4V_1$  at high sideslip angles and a Mach number of 9.6 are presented in figure 22. At both  $M = 6.8$  (fig. 21) and  $M = 9.6$  (fig. 22) the slope  $C_{n\beta}$  is about zero at sideslip angles above about  $5^\circ$ . This change in slope of the  $C_n$  curve for this cranked-wing configuration is most severe at  $M = 9.6$ . Again by referring back to the schlieren flow photographs presented in figure 3(c), it is noted that the body shock crosses the downwind vertical-tip fin at a sideslip angle of about  $5^\circ$  and lies outboard of it at higher sideslip angles. Thus, when the body shock lies

[REDACTED]

inboard or impinges on the tip fin, increased  $C_{n\beta}$  or fin effectiveness results. After the shock moved outboard of the fin, the inputs to  $C_{n\beta}$  due to shock impingement were no longer existent and also the local flow angle of the fin was reduced; thus, the effectiveness and  $C_{n\beta}$  decreased. This effect of shock position upon  $C_{n\beta}$  is similar to the effects of shock position upon  $C_{n\beta}$  because of the change in Mach number discussed previously.

#### CONCLUDING REMARKS

An investigation has been conducted at the Langley Research Center to study the effects of wing plan-form geometry on some of the aerodynamic characteristics of a hypersonic glider at Mach numbers from subsonic up to 9.6. From an analysis of the data obtained during this investigation, it is noted that the rearward shifts of the location of the aerodynamic center and center of pressure at transonic speeds were less for the configurations with body and wing apexes coincident. At a Mach number of 9.6, the aerodynamic center is slightly rearward of the location at subsonic speeds, whereas the center of pressure has moved forward of its subsonic location.

Moving the centroid of area rearward (and thus the center of pressure) by cranking the wing leading edge increased the longitudinal stability throughout the Mach number range of the tests for the configurations with the wing and body vertex coincident. However, with the wing moved rearward on the body and with the centroid of area displaced forward slightly by cranking the leading edge, a loss of stability at Mach numbers above about 3 resulted.

The local flow conditions in the region of the fins had a strong influence upon the directional stability of the configurations. Whenever the body shock moved outboard of the tip fins as a result of either a reduction in Mach number or an increase in sideslip angle, the fin effectiveness was reduced and the directional stability of the vehicle was likewise reduced.

At hypersonic speeds the cranked-wing vehicle with the body shock inboard of the tip fins had higher  $C_{n\beta}$  than the uncranked vehicle at

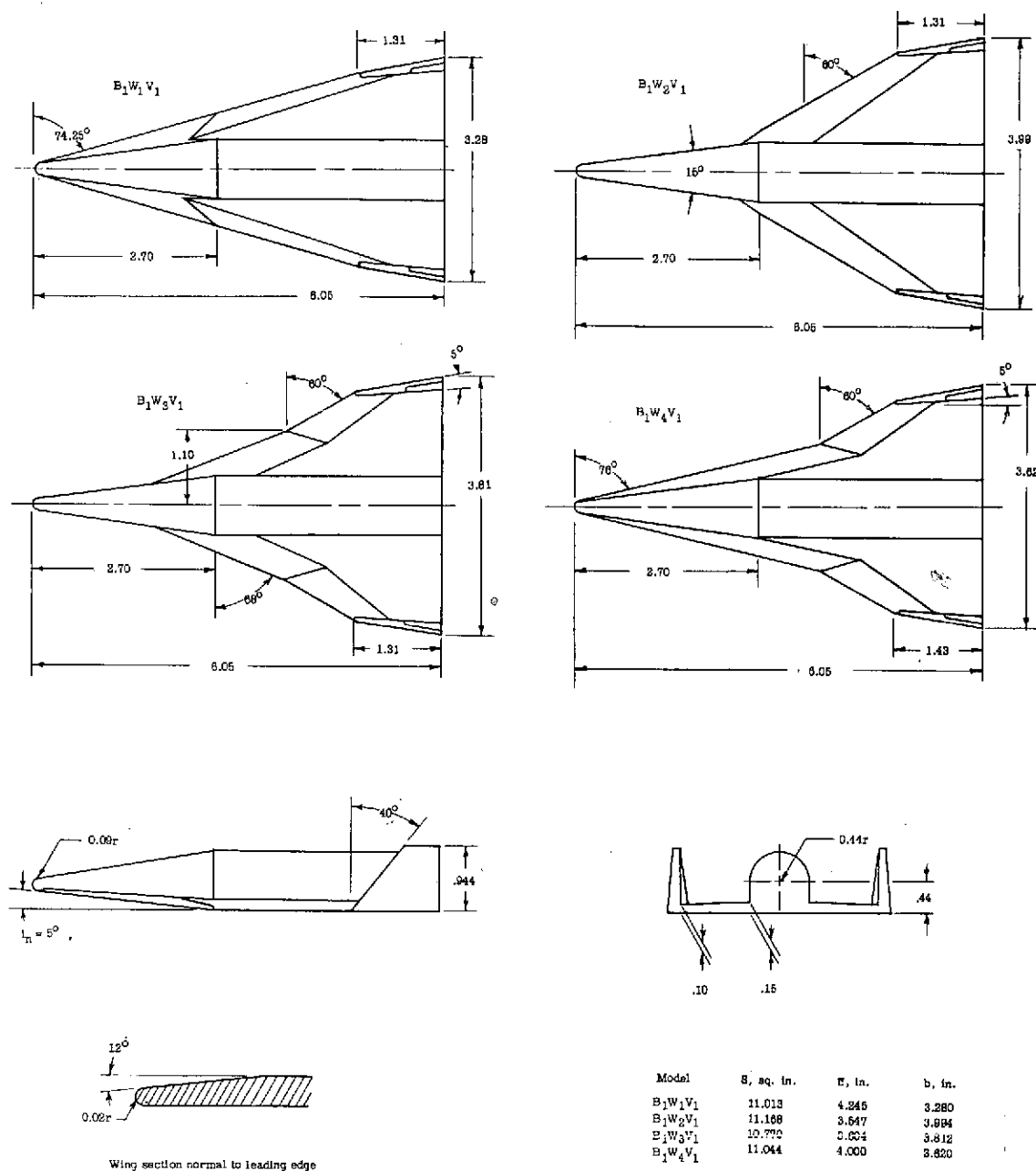
[REDACTED]

$\alpha = 0^\circ$  but the fall-off at the highest angles of attack was more severe for the crank-wing vehicle.

Langley Research Center,  
National Aeronautics and Space Administration,  
Langley Field, Va., February 18, 1960.

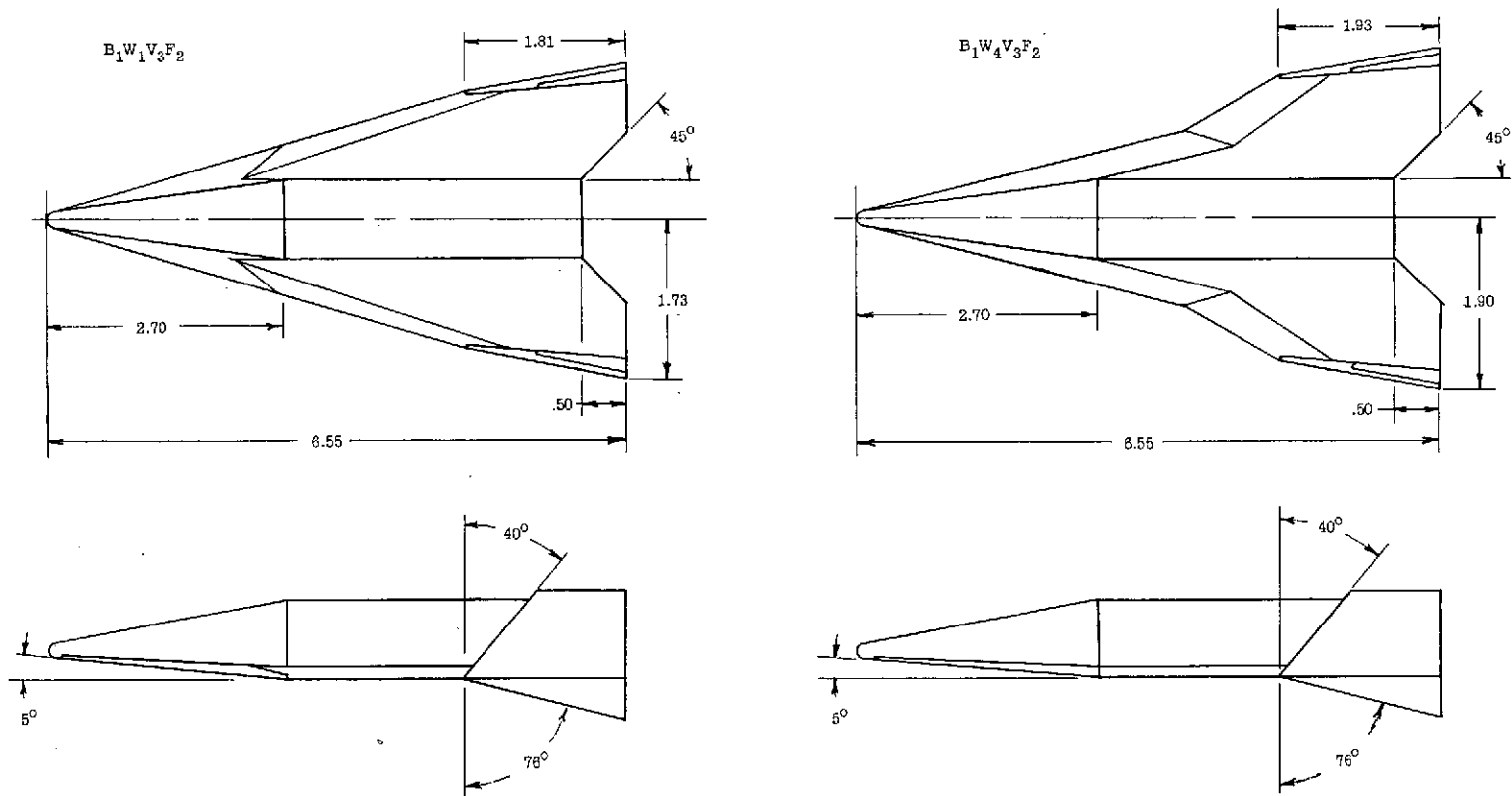
#### REFERENCES

1. Shanks, Robert E.: Effect of Wing Crank and Sweepback on the Low Subsonic Stability and Control Characteristics of a Model of a Hypersonic Boost-Glide Type Airplane. NASA TM X-181, 1960.
2. West, Franklin E., Jr., Trescot, Charles D., Jr., and Wiley, Alfred N., Jr.: Aerodynamic Characteristics for Two Hypersonic Glider Models With and Without Wing and Vertical-Tail Trailing-Edge Chord-Extensions at a Mach Number of 0.94. NASA TM X-66, 1960.
3. Rainey, Robert W., Fetterman, David E., Jr., and Smith, Robert: Summary of the Static Stability and Control Results of a Hypersonic Glider Investigation. NASA TM X-277, 1960.
4. McLellan, Charles H., and Ladson, Charles L.: A Summary of the Aerodynamic Performance of Hypersonic Gliders. NASA TM X-237, 1960.
5. Rainey, Robert W.: Static Stability and Control of Hypersonic Gliders. NACA RM L58E12a, 1958.



(a) Basic models.

Figure 1.- Three-view drawings of models tested. All linear dimensions are in inches.

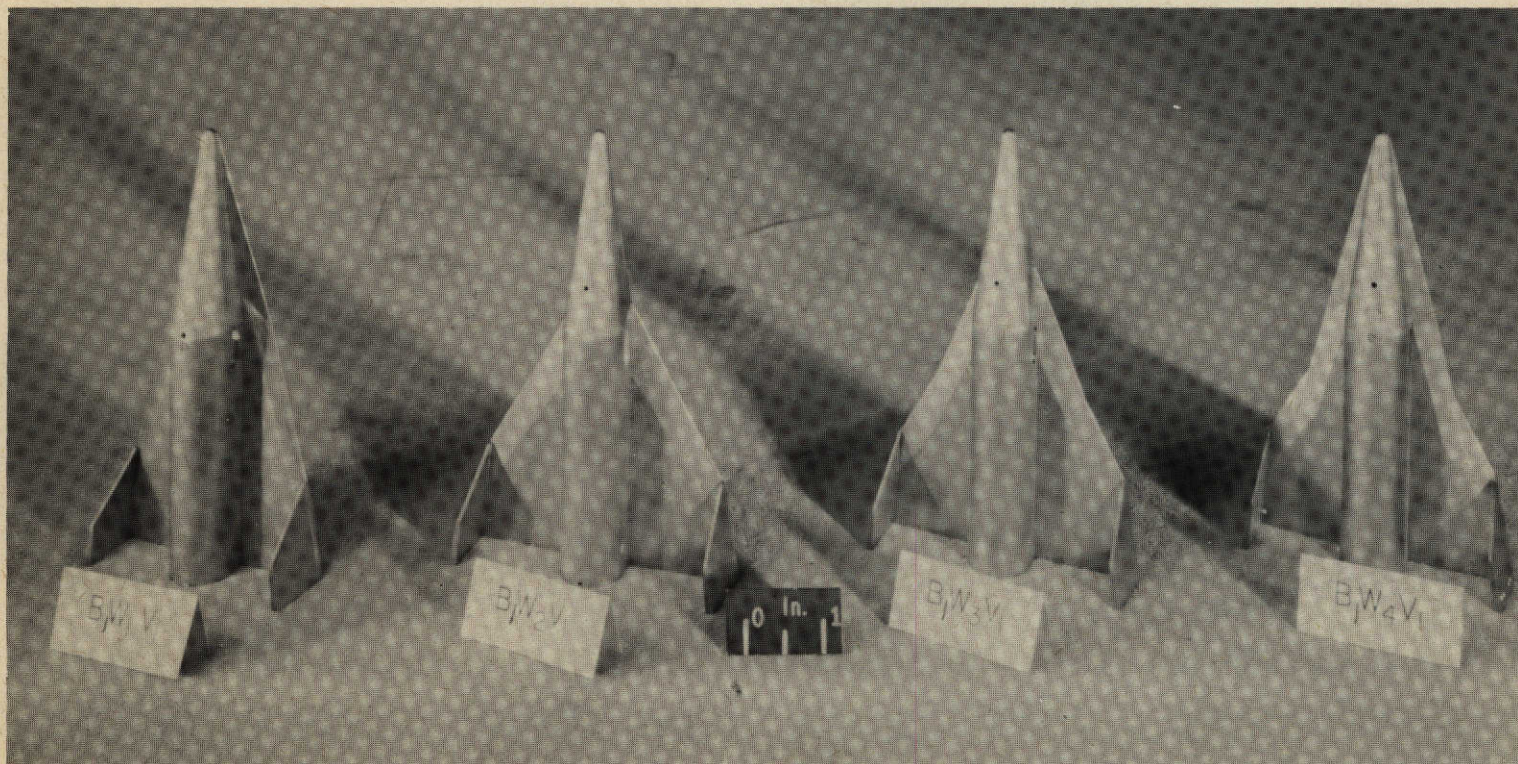


| Model          | S, sq in. | $\bar{c}$ , in. | b, in. |
|----------------|-----------|-----------------|--------|
| $B_1W_1V_3F_2$ | 12.018    | 4.274           | 3.458  |
| $B_1W_4V_3F_2$ | 12.212    | 4.019           | 3.798  |

(b) Alterations to basic models.

Figure 1.- Concluded.



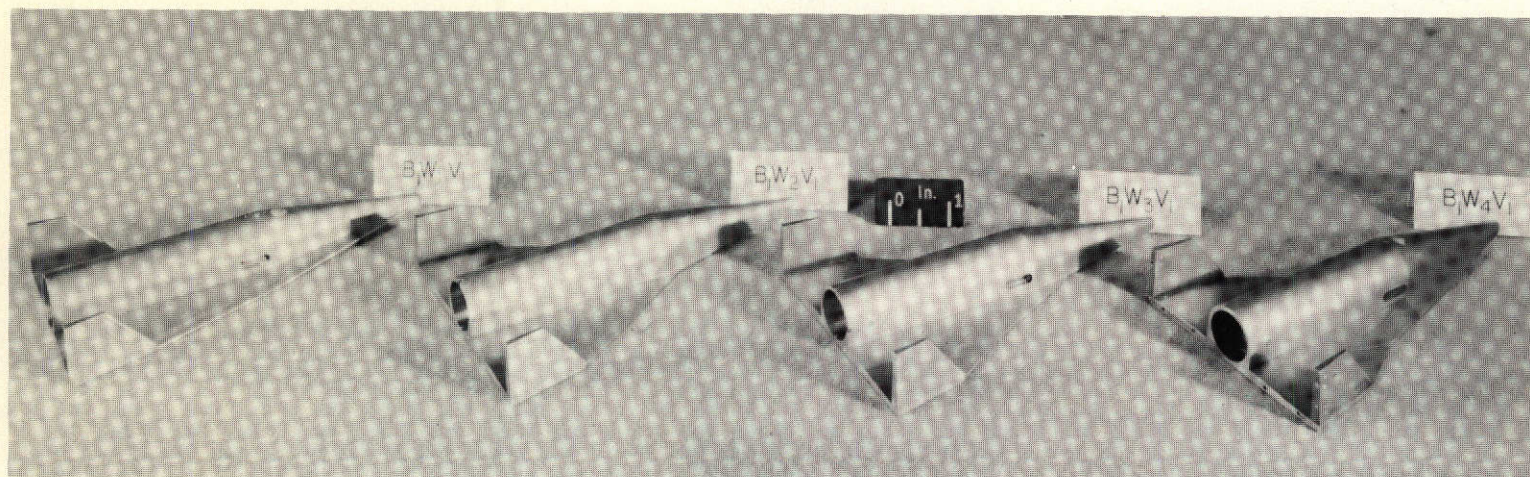


(a) Top view.

L-58-236a.1

Figure 2.- Model photographs.





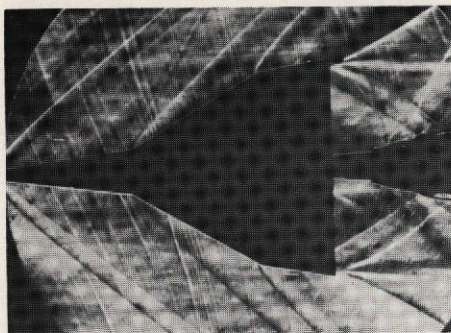
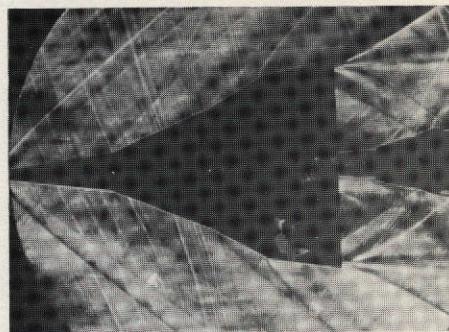
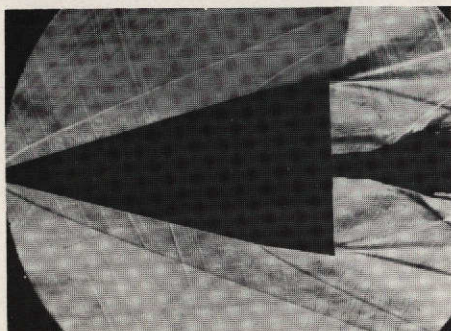
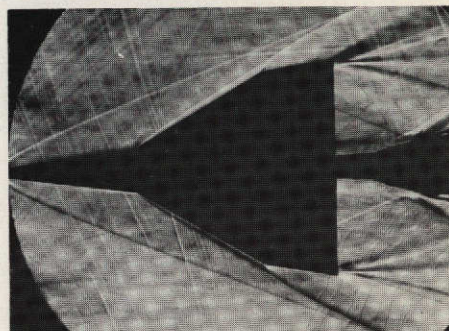
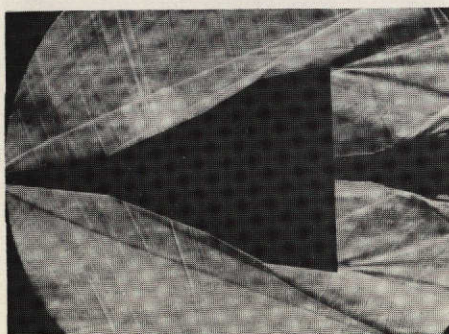
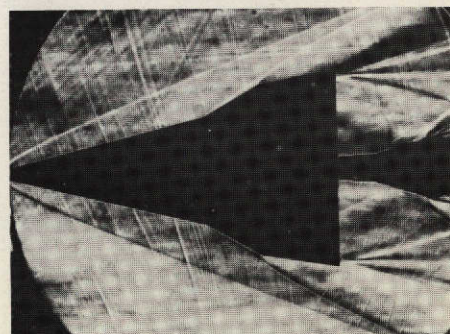
(b) Side view.

L-58-238a.1

Figure 2.- Concluded.



CONFIDENTIAL

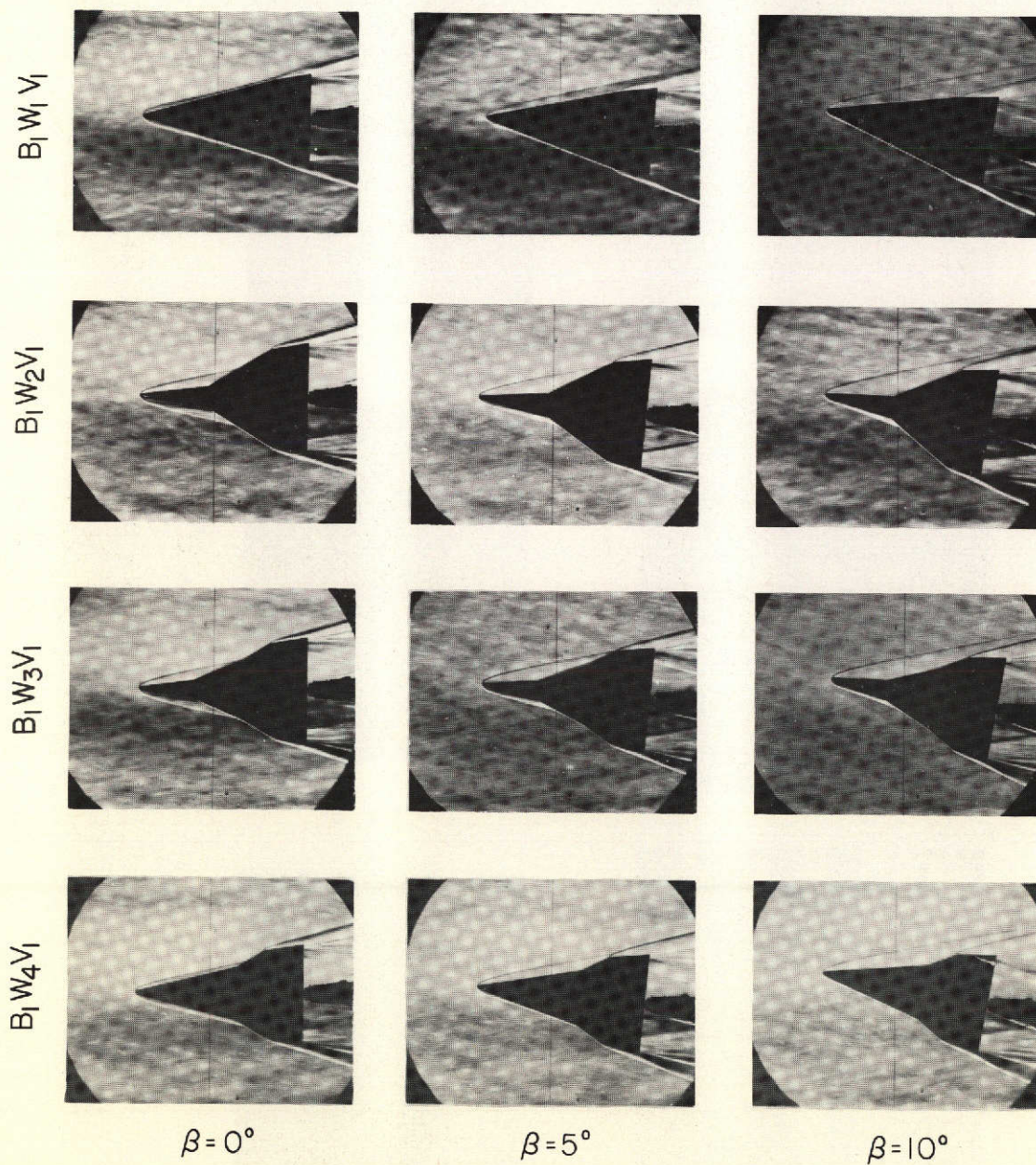
 $B_1 W_2 V_1$  $B_1 W_3 V_1$ (a)  $M = 1.62$ ;  $\beta = 0^\circ$ ;  $\alpha = 0^\circ$ . $B_1 W_1 V_1$  $B_1 W_2 V_1$  $B_1 W_3 V_1$  $B_1 W_4 V_1$ (b)  $M = 2.91$ ;  $\beta = 0^\circ$ ;  $\alpha = 0^\circ$ .

L-60-255

Figure 3.- Schlieren flow photographs.

CONFIDENTIAL





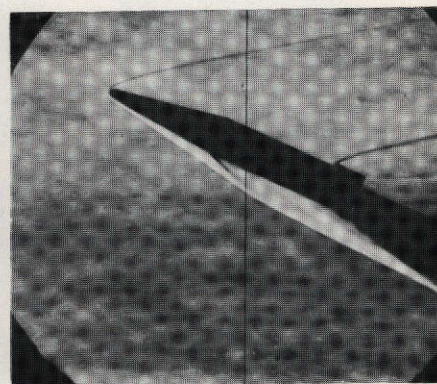
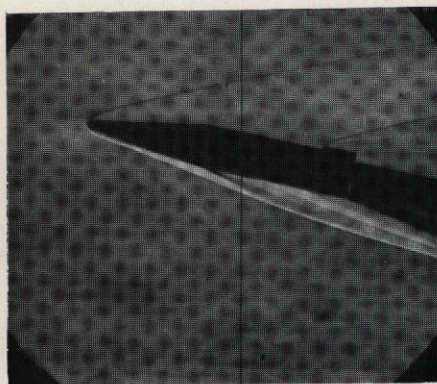
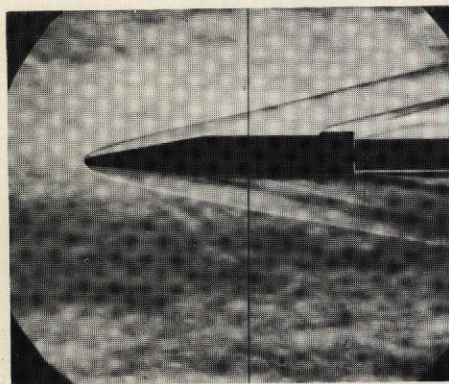
(c)  $M = 6.8$ ;  $\alpha = 0^\circ$ .

L-60-256

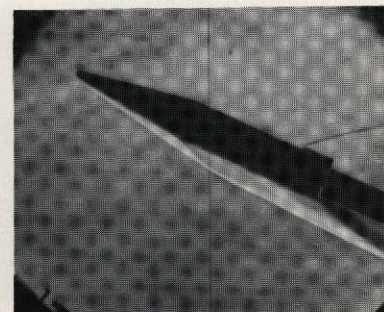
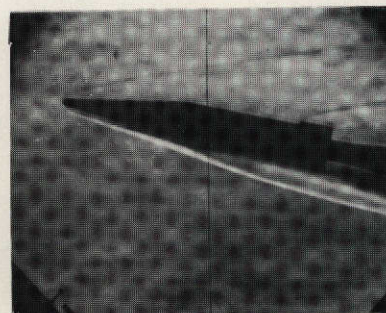
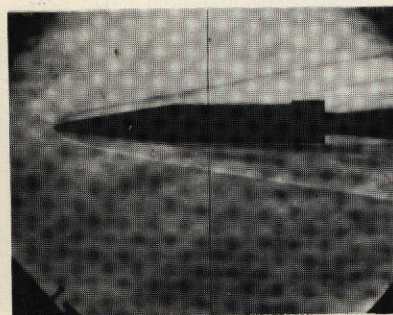
Figure 3.- Continued.



M = 6.8



M = 9.6

 $\alpha = 0^\circ$  $\alpha = 12^\circ$  $\alpha = 24^\circ$ (a)  $\beta = 0^\circ$ .

L-60-257

Figure 3.- Concluded.

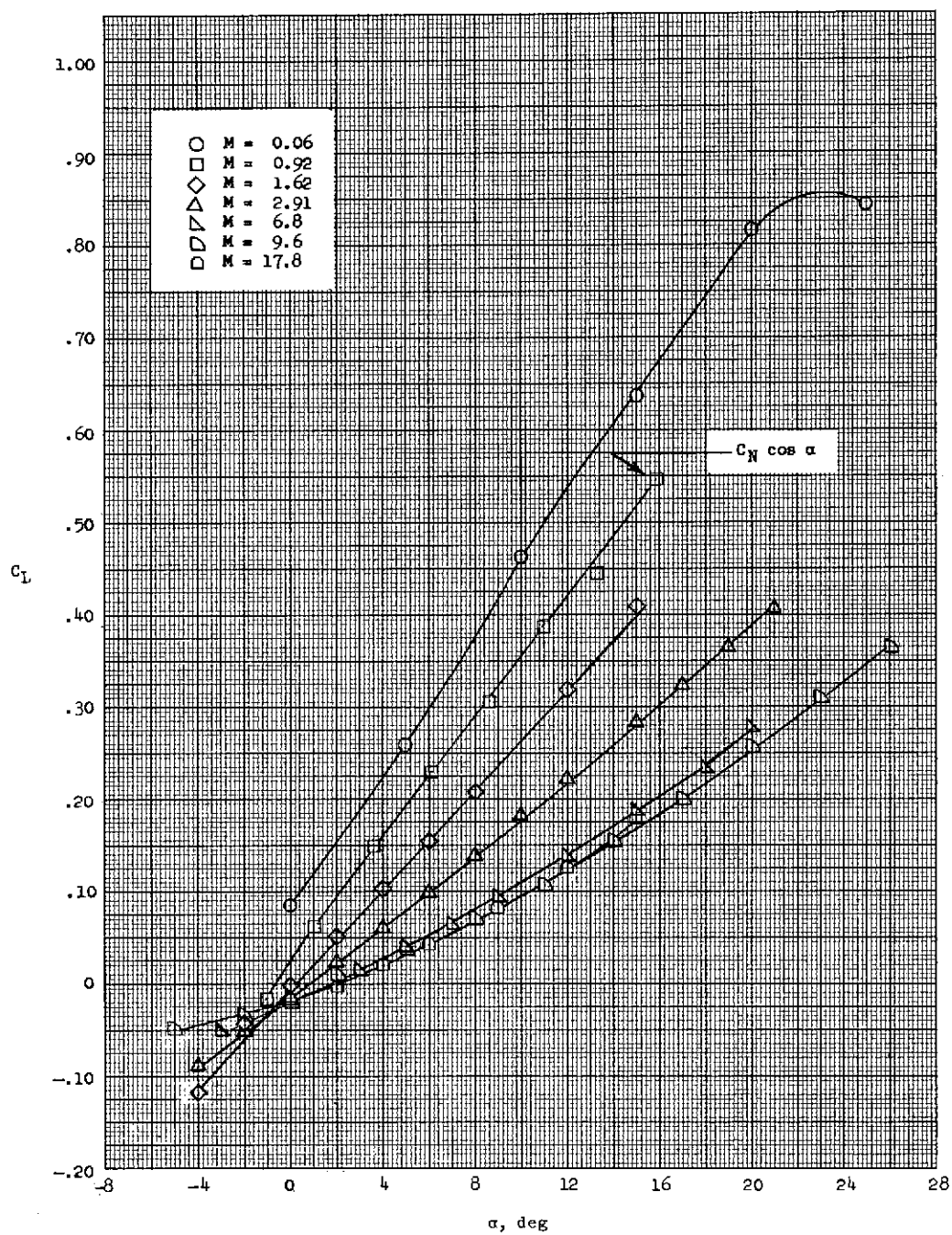
(a) Model  $B_1W_1V_1$ .

Figure 4.- Lift coefficient plotted against angle of attack for all Mach numbers of the test.



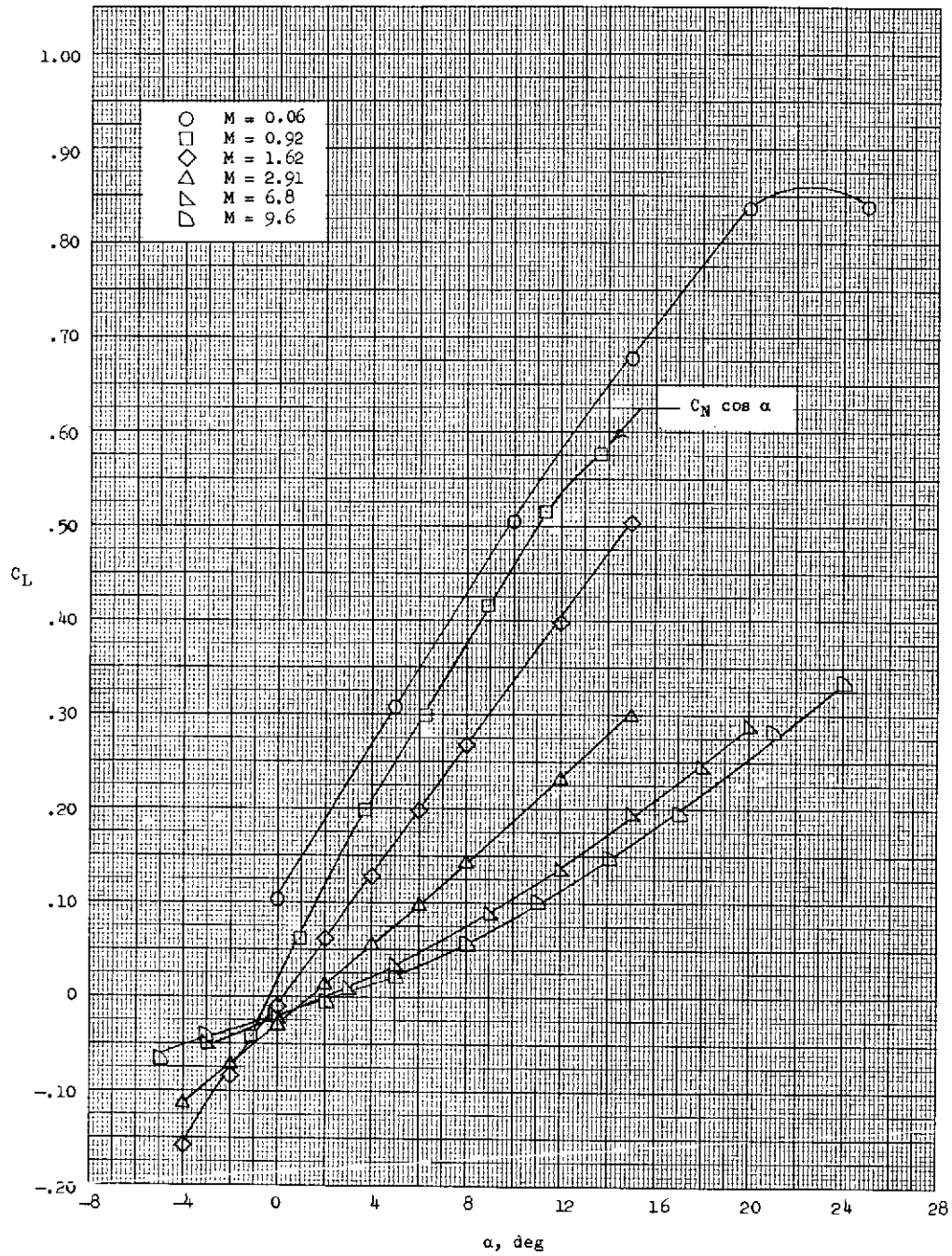
(b) Model  $B_1W_2V_1$ .

Figure 4.- Continued.

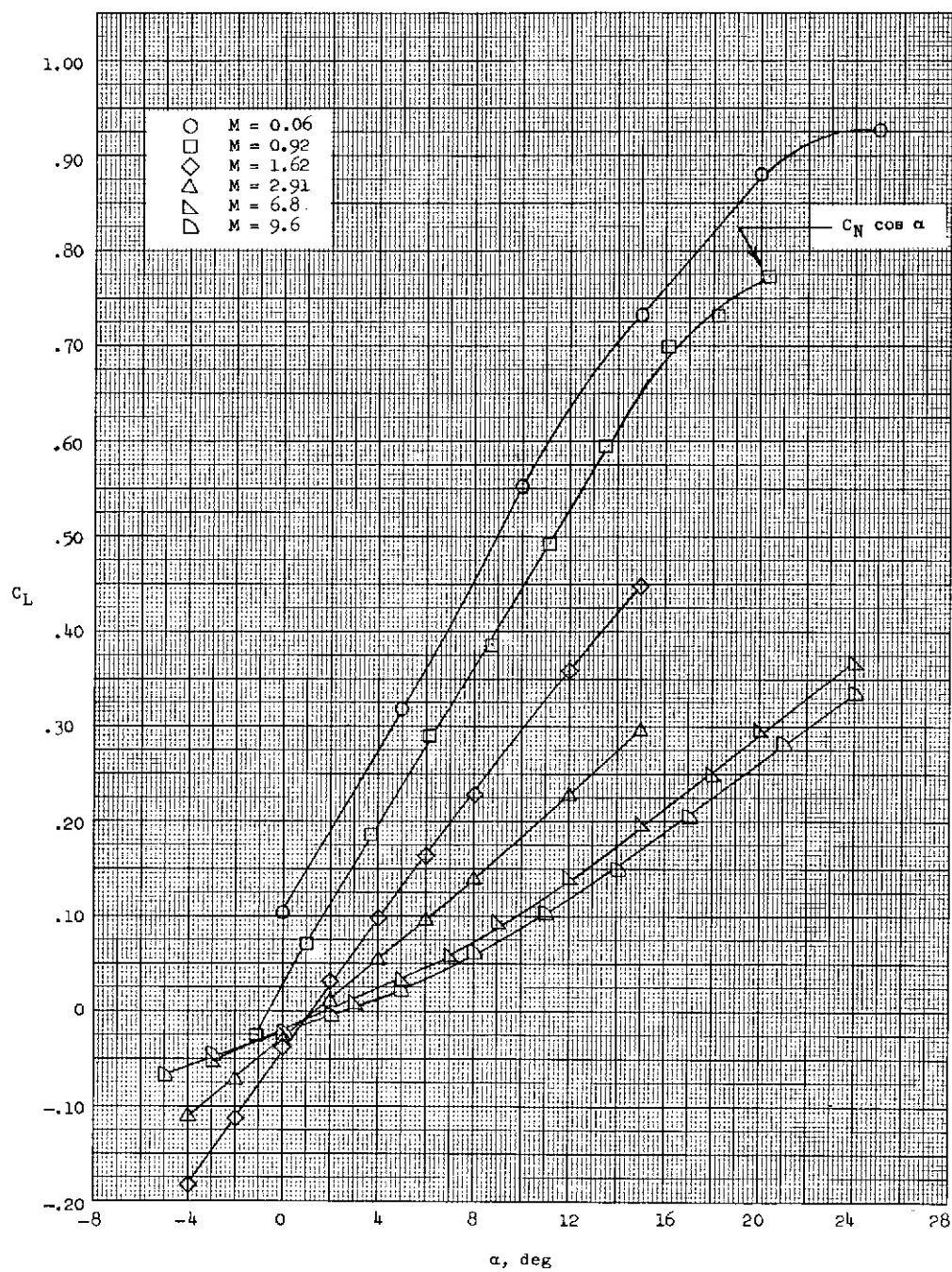
(c) Model  $B_1W_3V_1$ .

Figure 4.- Continued.



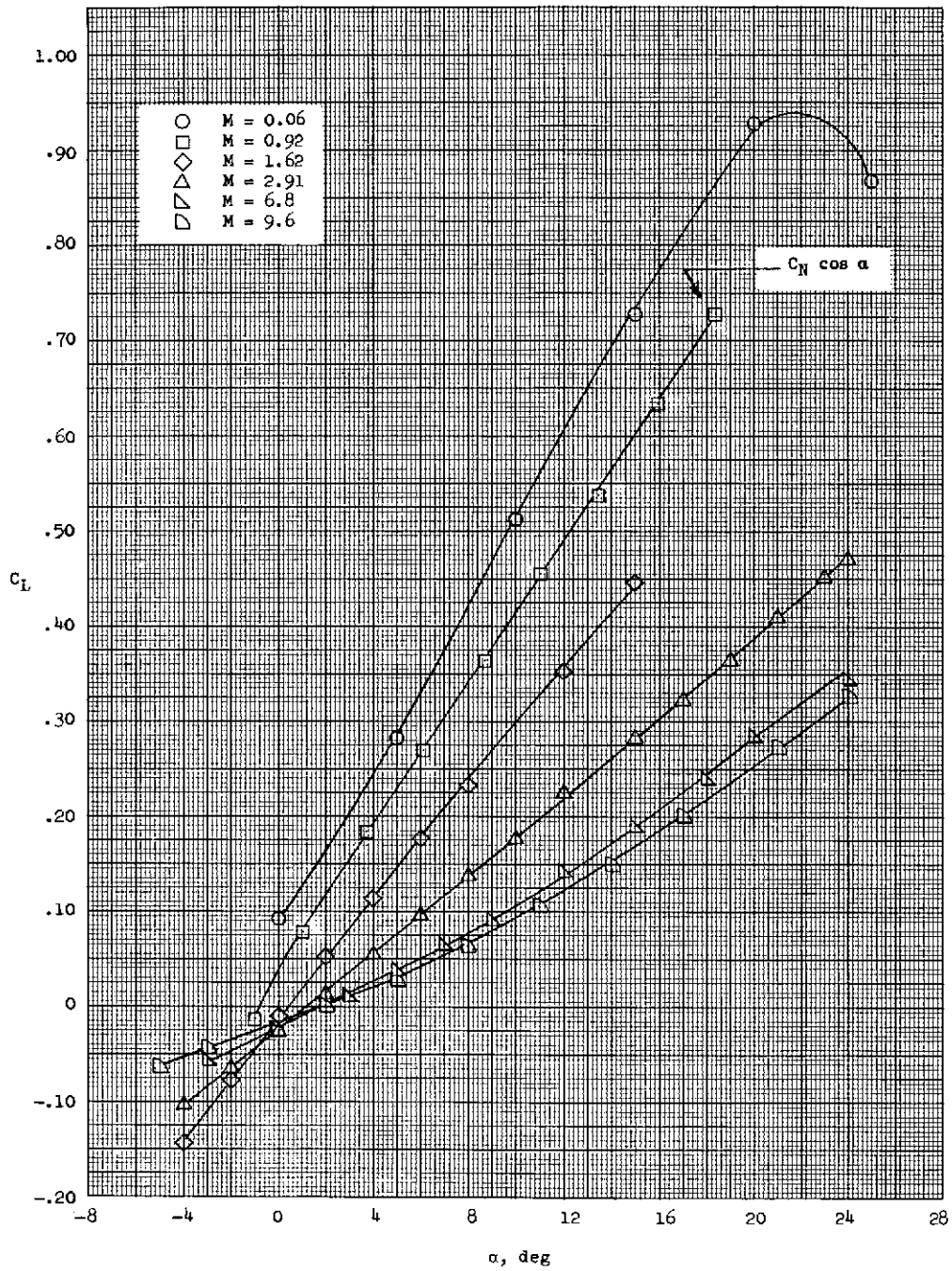
(d) Model B<sub>1</sub>W<sub>4</sub>V<sub>1</sub>.

Figure 4.- Continued.

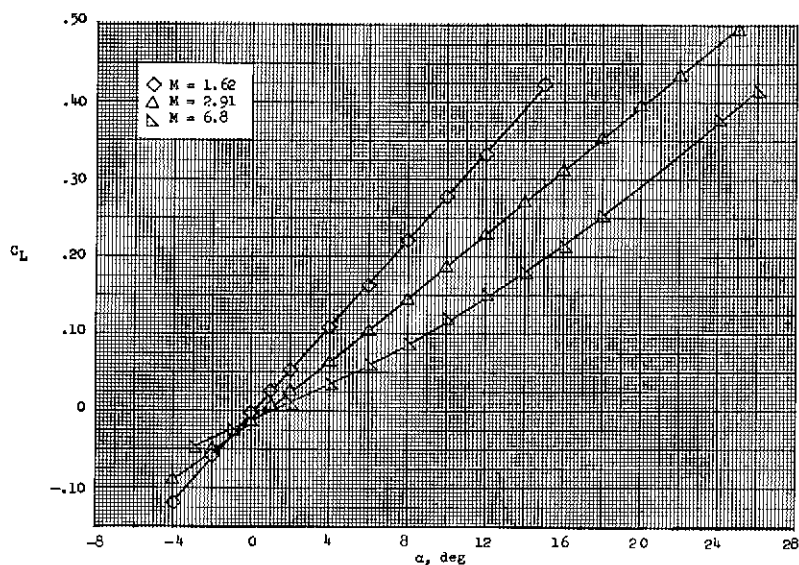
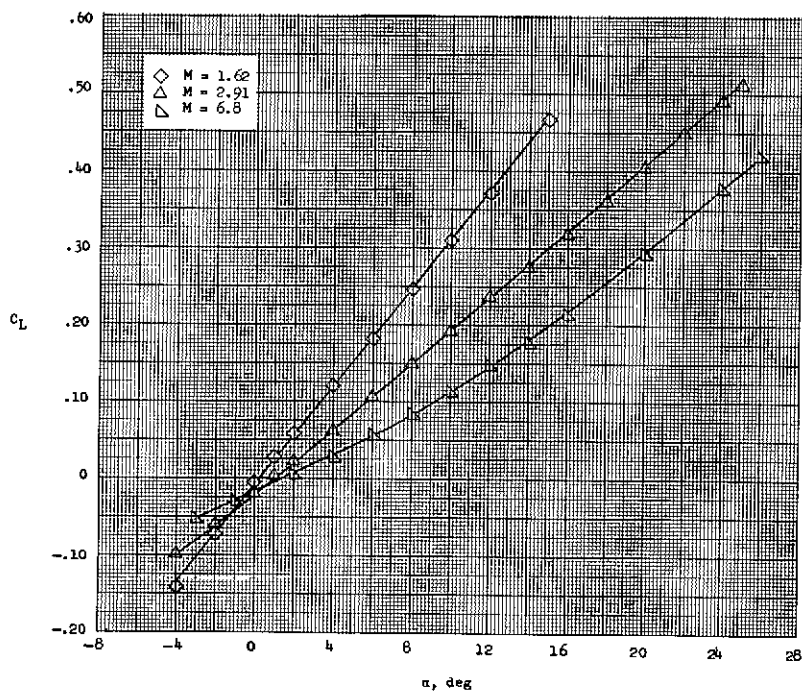
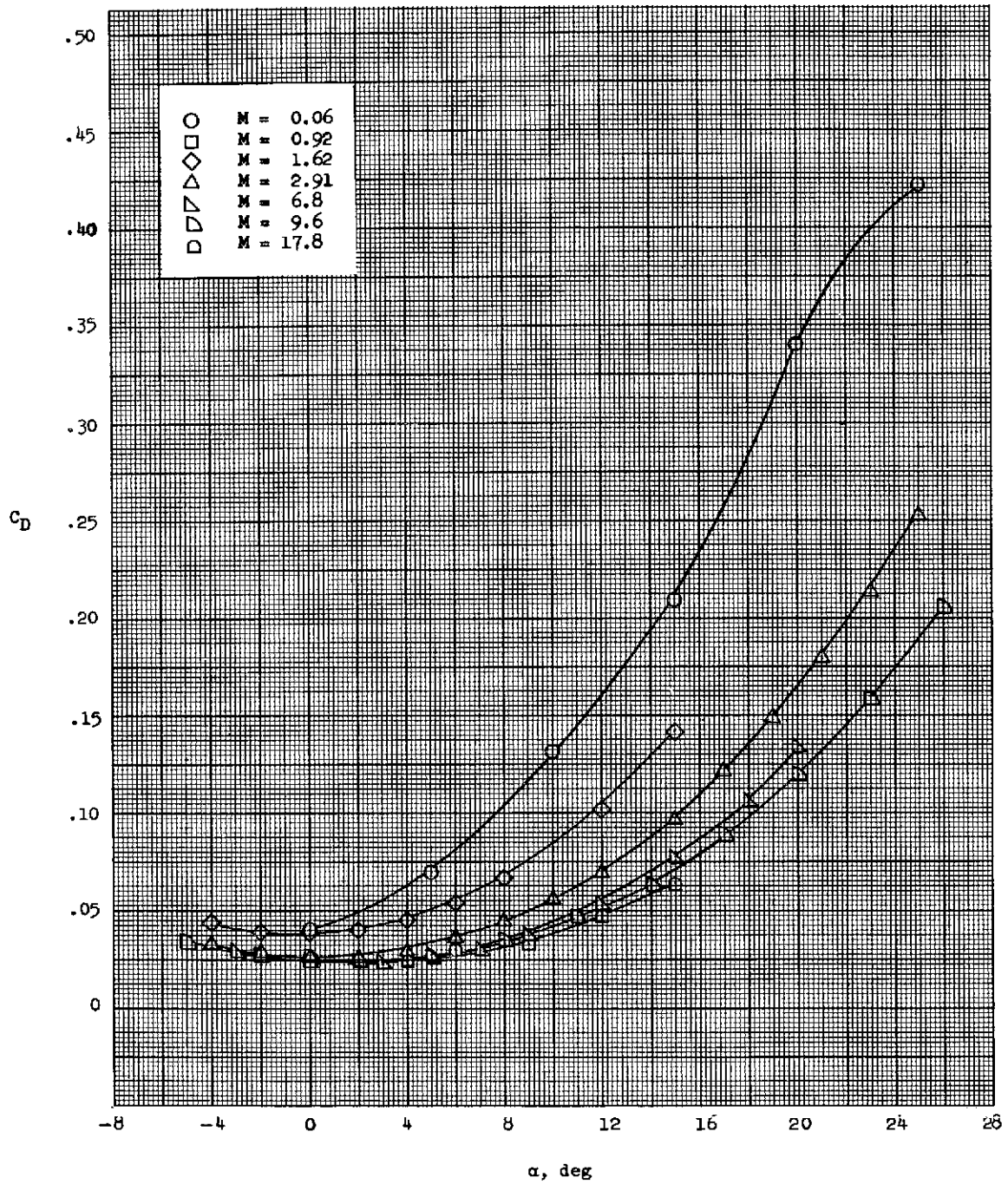
(e) Model  $B_1W_1V_3F_2$ .(f) Model  $B_1W_4V_3F_2$ .

Figure 4.- Concluded.



(a) Model B<sub>1</sub>W<sub>1</sub>V<sub>1</sub>.

Figure 5.- Drag coefficient as a function of angle of attack for all Mach numbers.

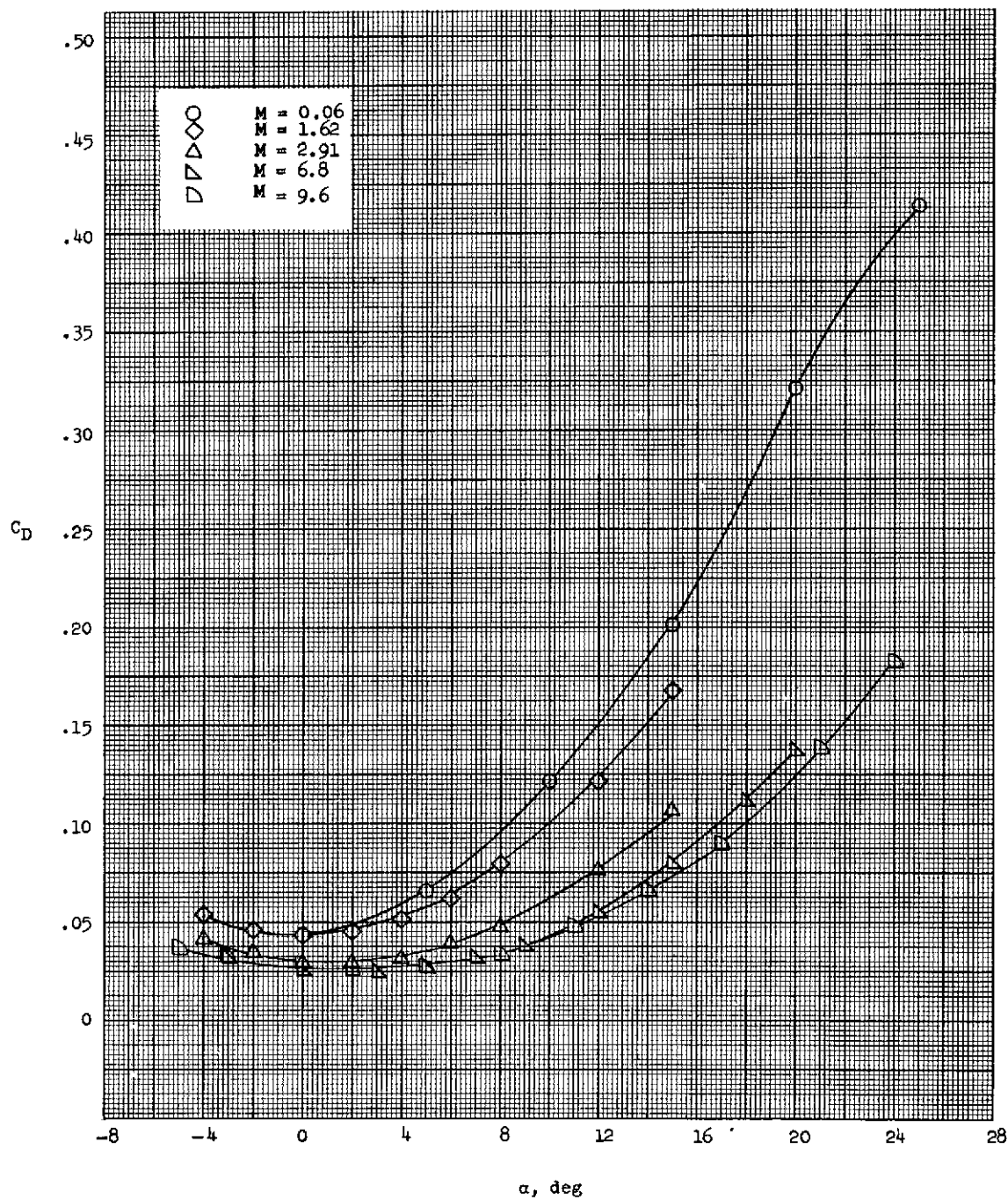
(b) Model  $B_1W_2V_1$ .

Figure 5.- Continued.

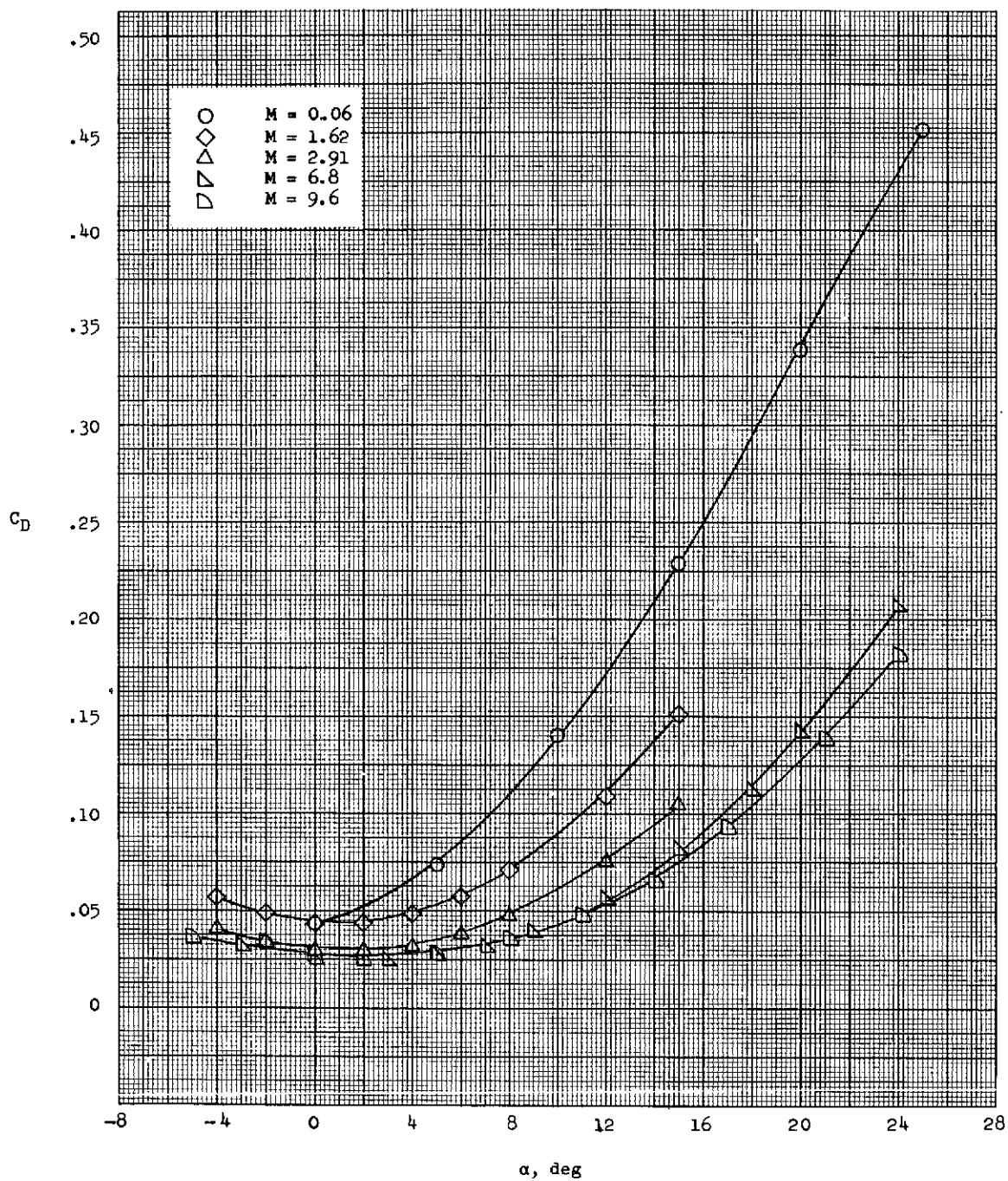
(c) Model  $B_1W_3V_1$ .

Figure 5.- Continued.

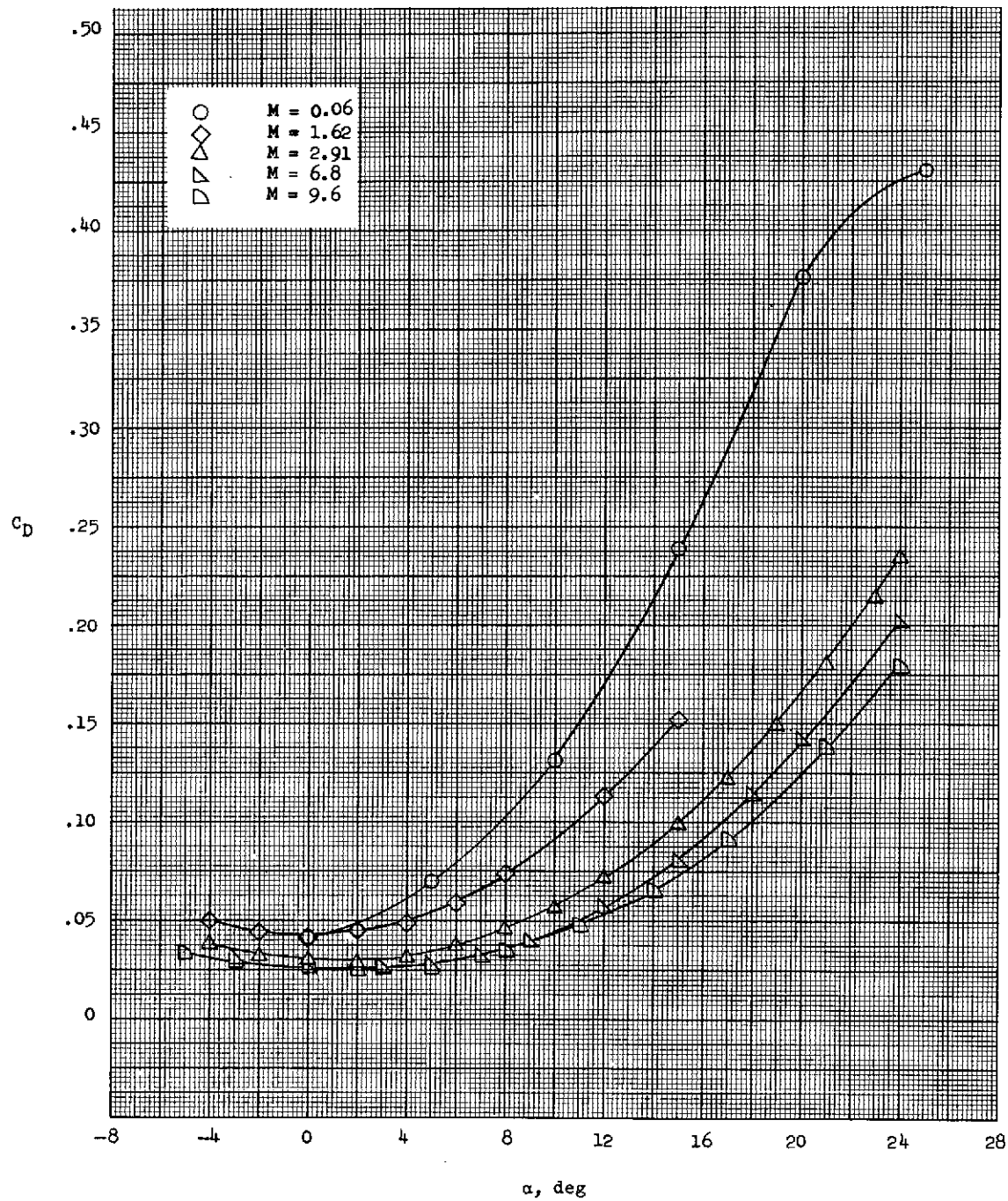
(d) Model  $B_1W_4V_1$ .

Figure 5.- Continued.



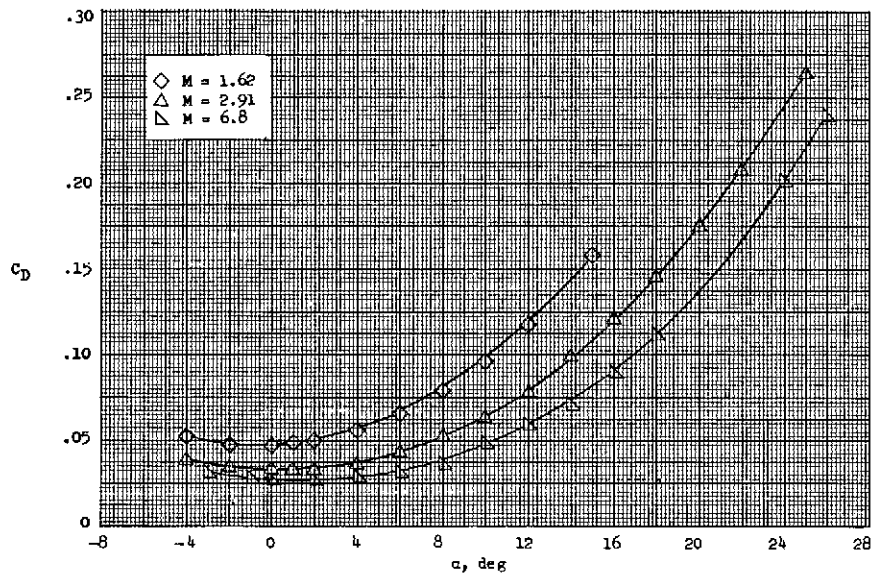
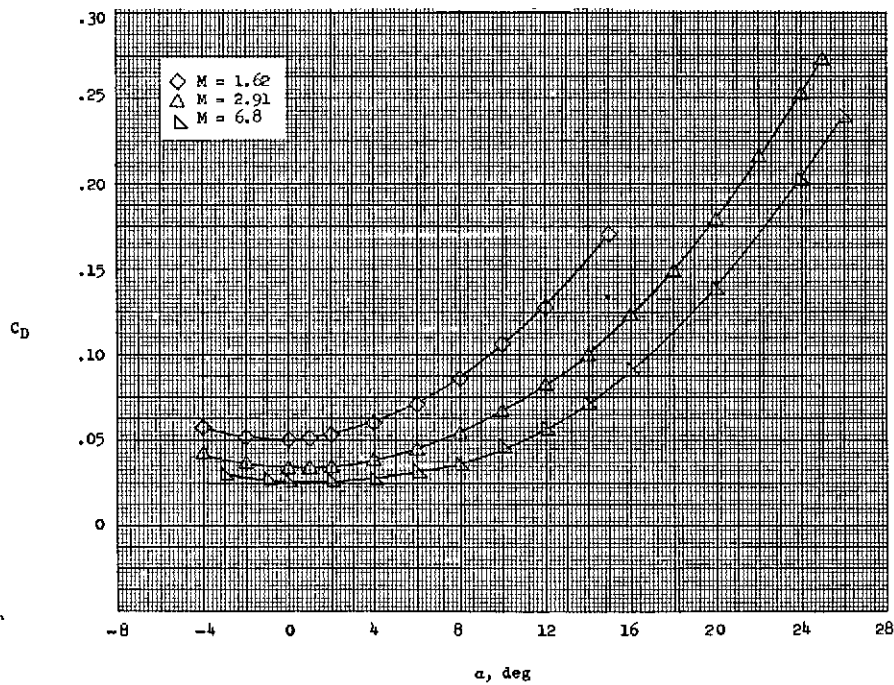
(e) Model  $B_1W_1V_3F_2$ .(f) Model  $B_1W_4V_3F_2$ .

Figure 5.- Concluded.

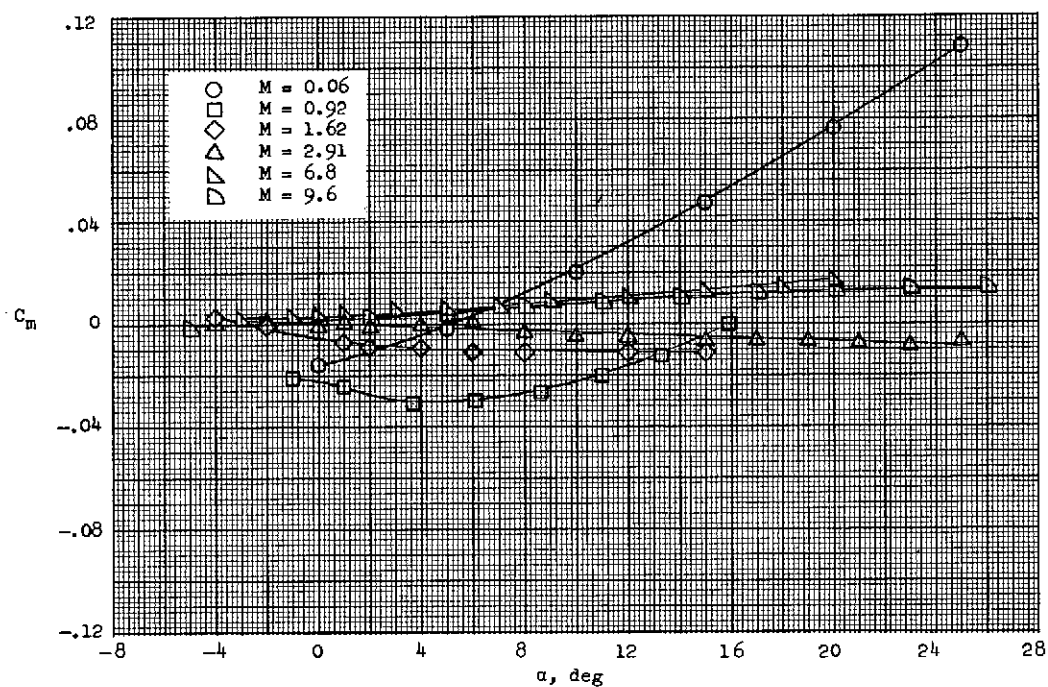
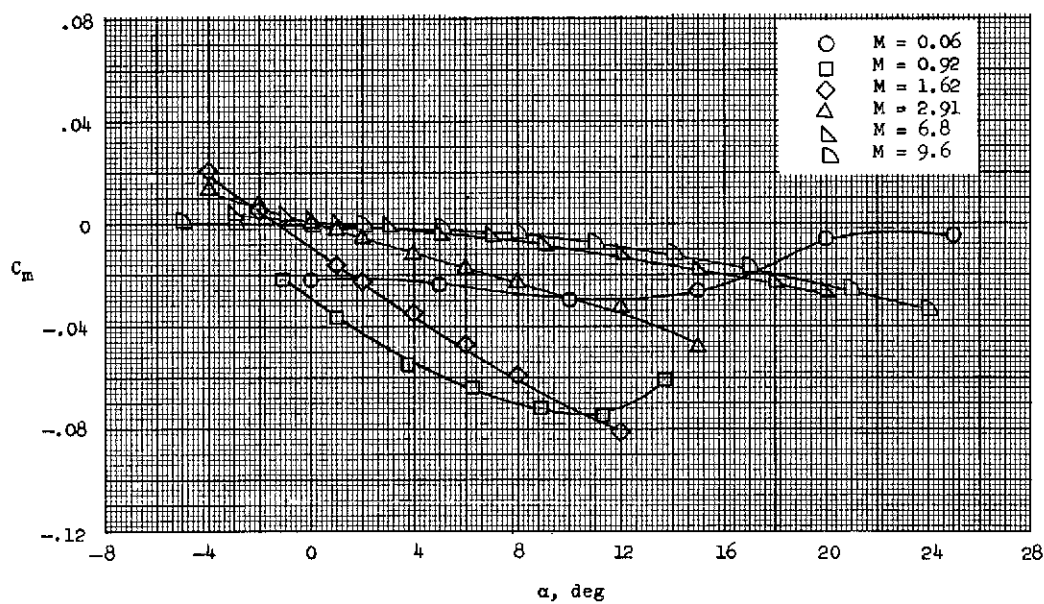
(a) Model  $B_1W_1V_1$ .(b) Model  $B_1W_2V_1$ .

Figure 6.- Pitching-moment coefficient plotted against angle of attack for all Mach numbers.



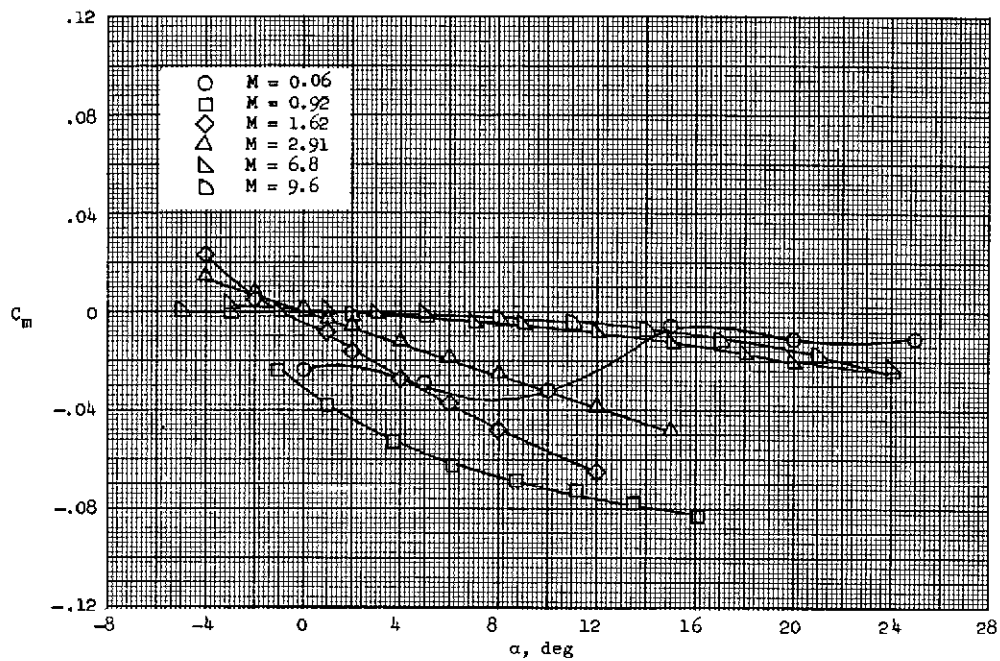
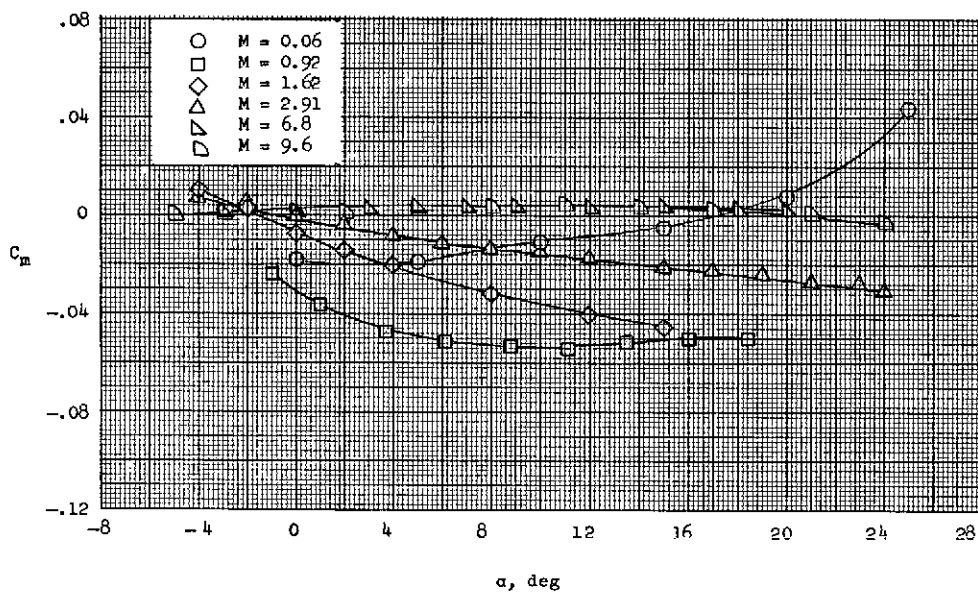
(c) Model  $B_1W_3V_1$ .(d) Model  $B_1W_4V_1$ .

Figure 6.- Continued.

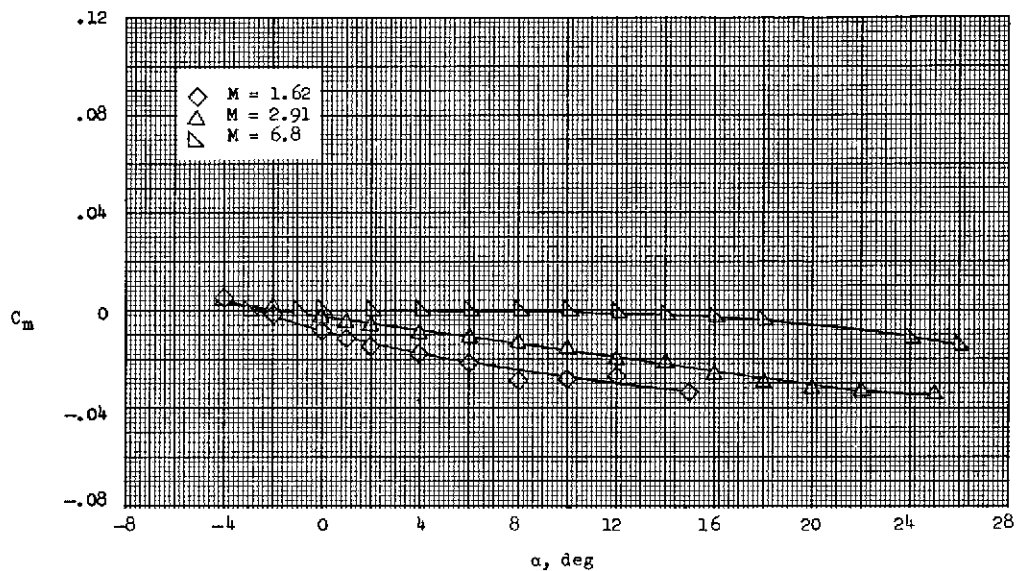
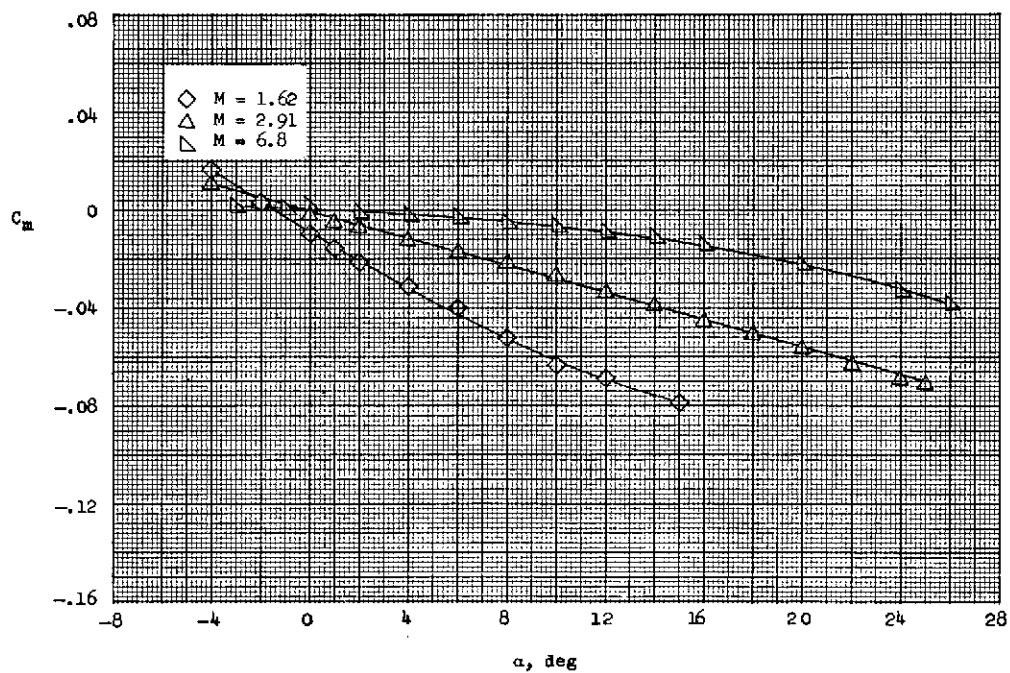
(e) Model  $B_1W_1V_3F_2$ .(f) Model  $B_1W_4V_3F_2$ .

Figure 6.- Concluded.

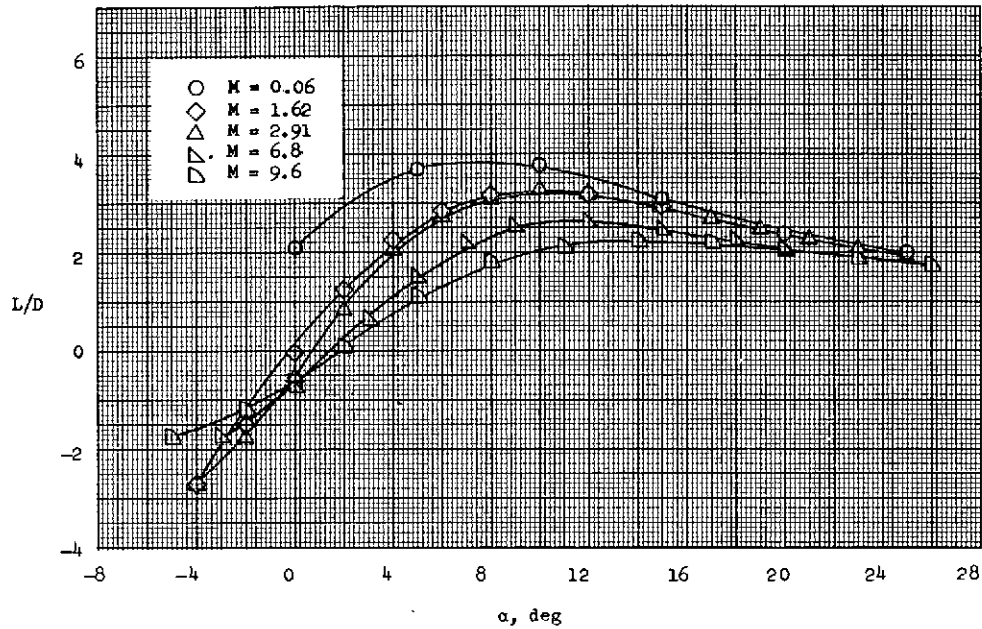
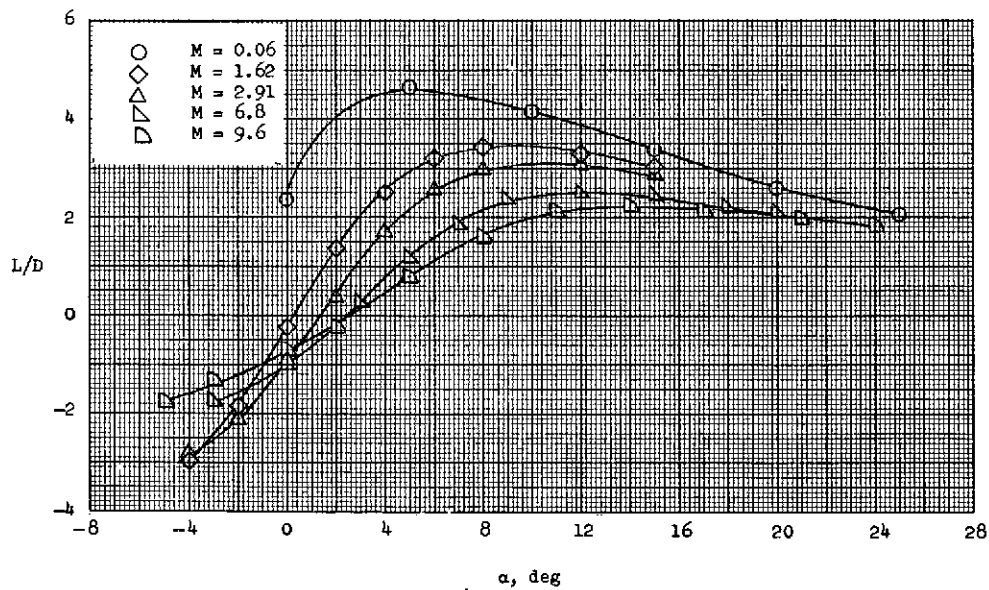
(a) Model  $B_1W_1V_1$ .(b) Model  $B_1W_2V_1$ .

Figure 7.- Lift-drag ratio plotted against angle of attack for several Mach numbers.

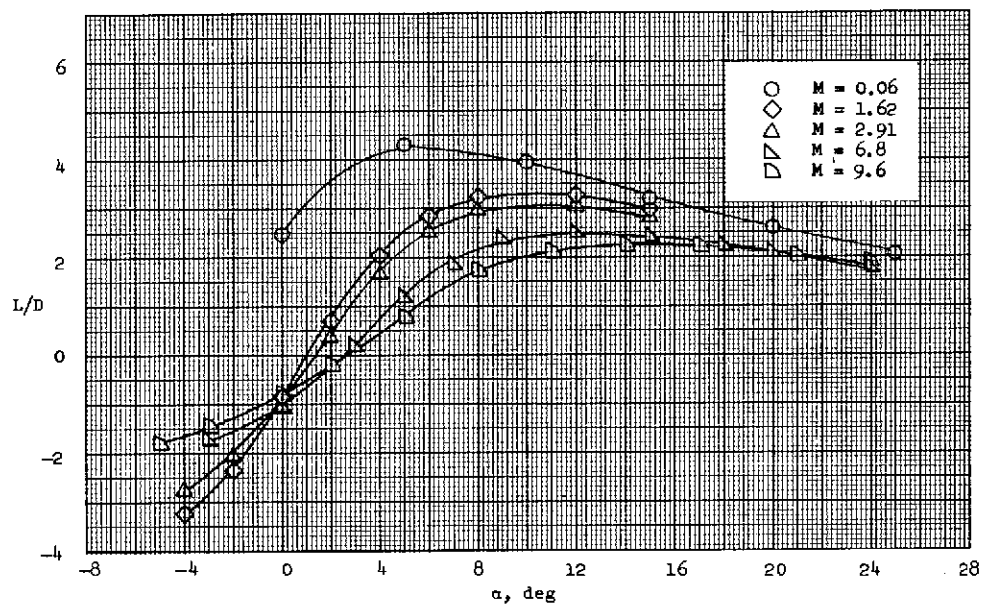
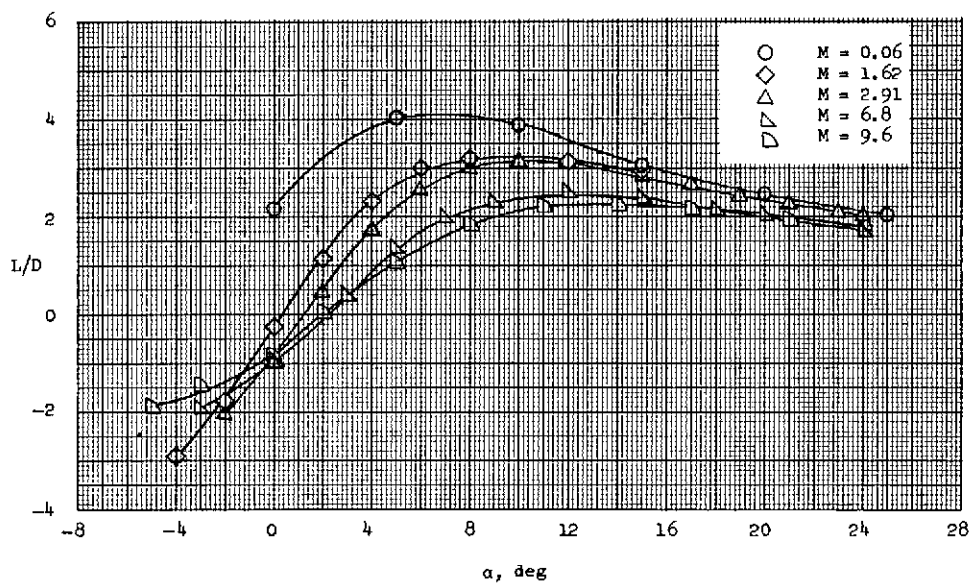
(c) Model  $B_1W_3V_1$ .(d) Model  $B_1W_4V_1$ .

Figure 7.- Continued.

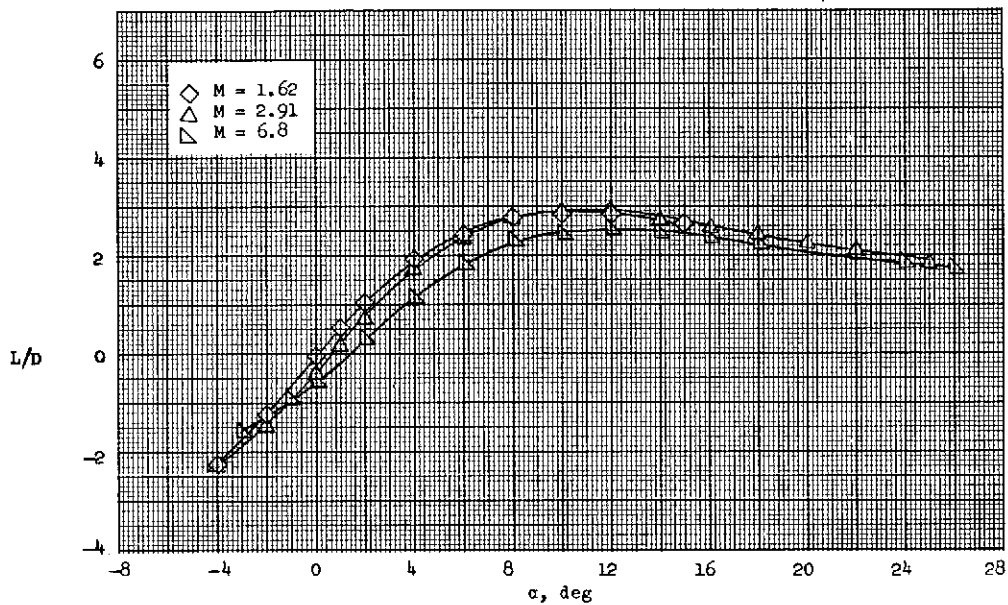
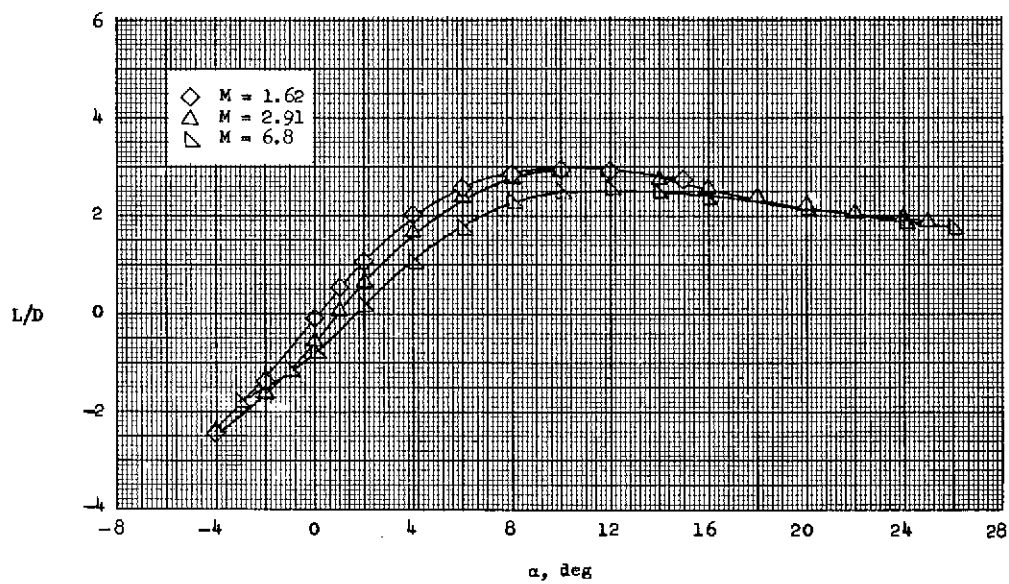
(e) Model  $B_1W_1V_3F_2$ .(f) Model  $B_1W_4V_3F_2$ .

Figure 7.- Concluded.



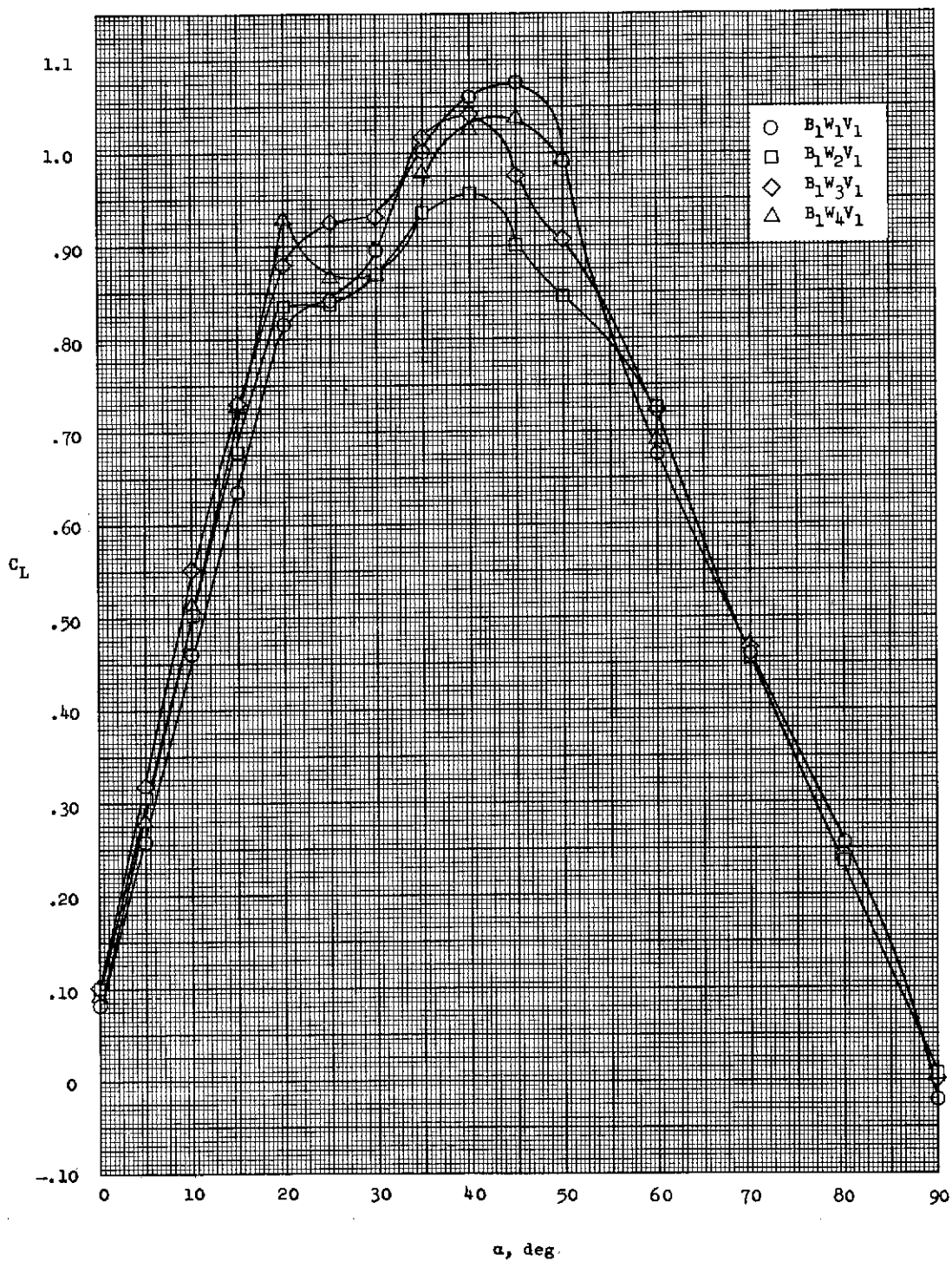


Figure 8.- Lift coefficient plotted against angle of attack.  $M = 0.06$ .

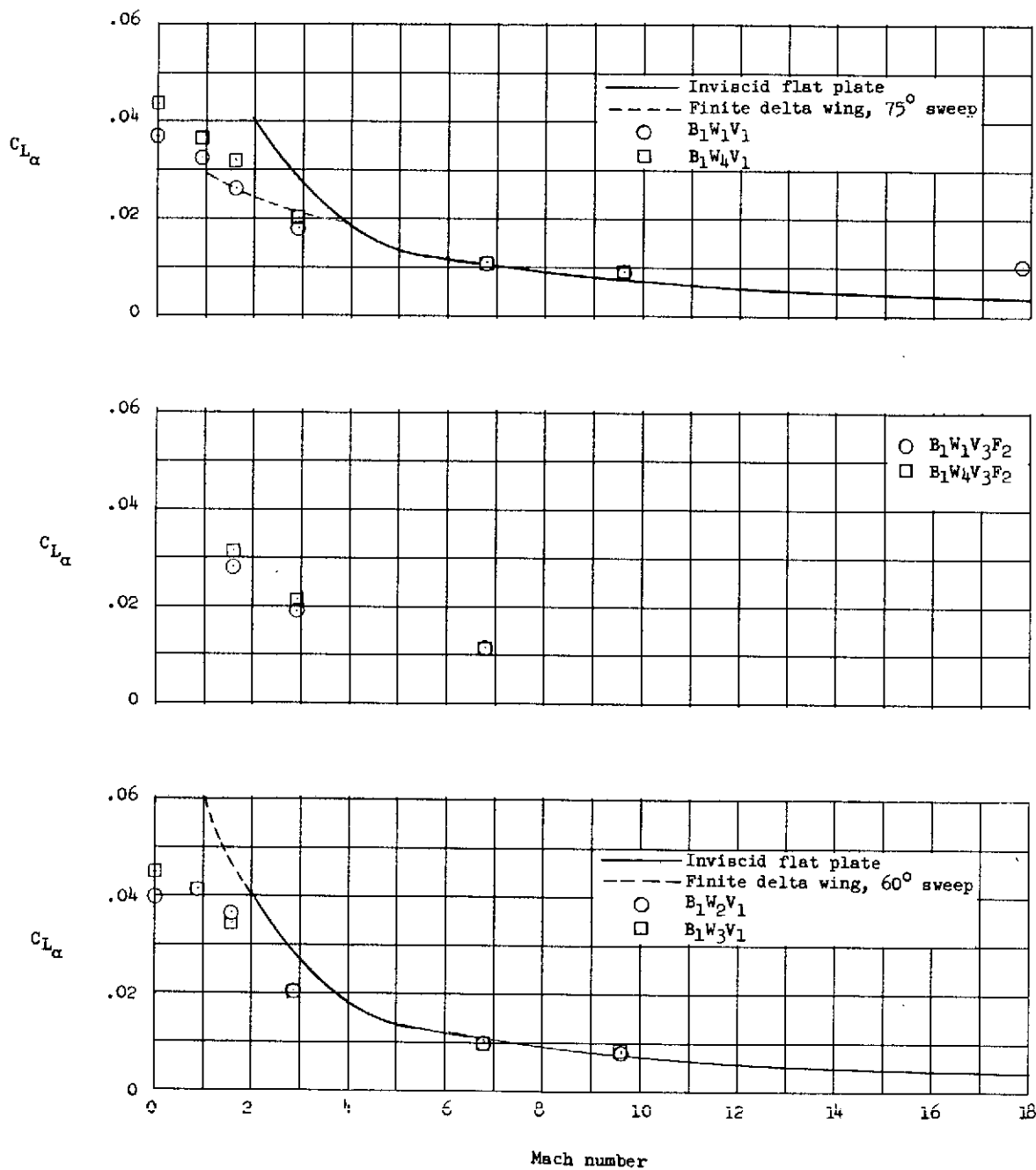


Figure 9.- Lift-curve slope plotted against Mach number.

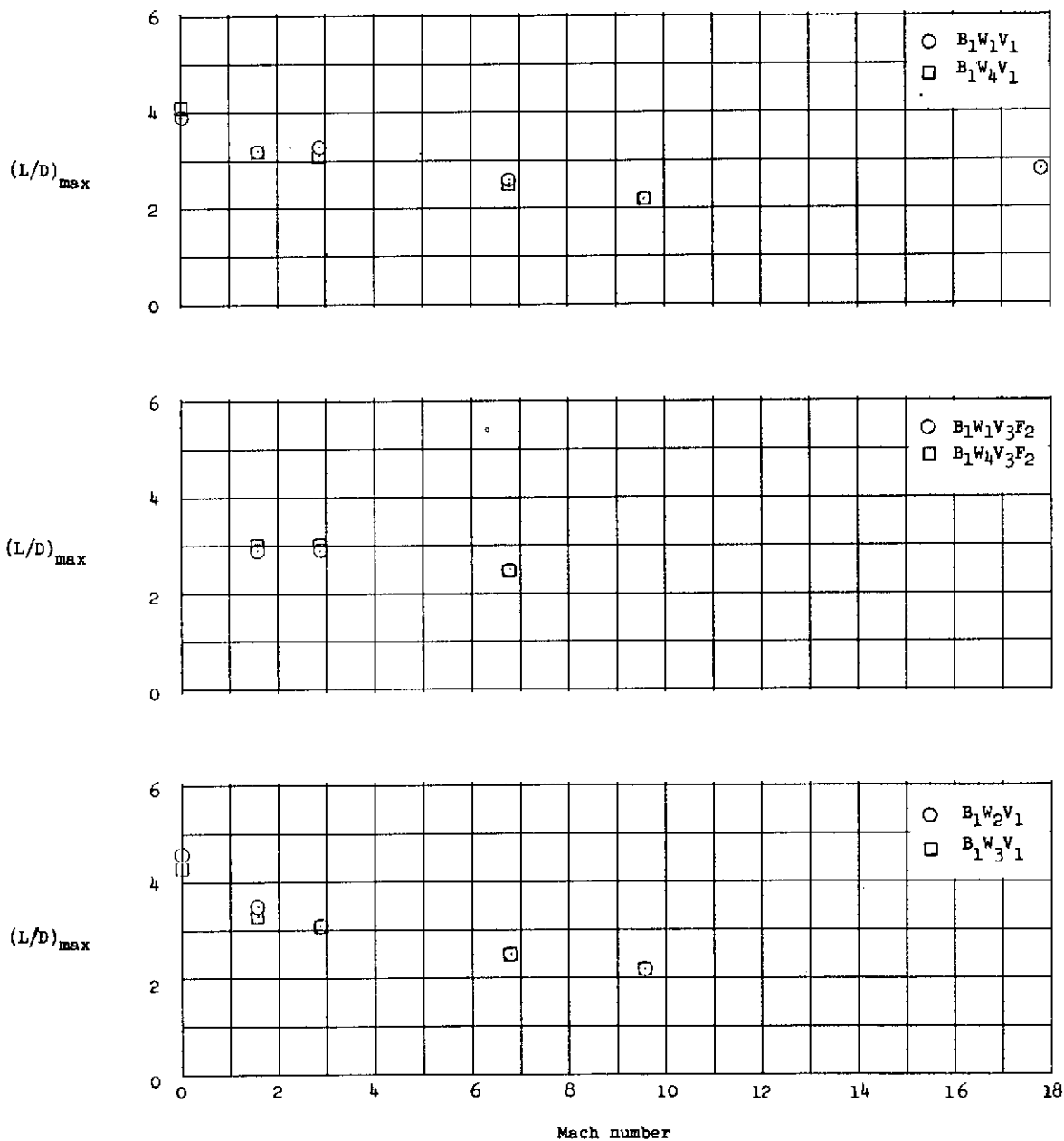
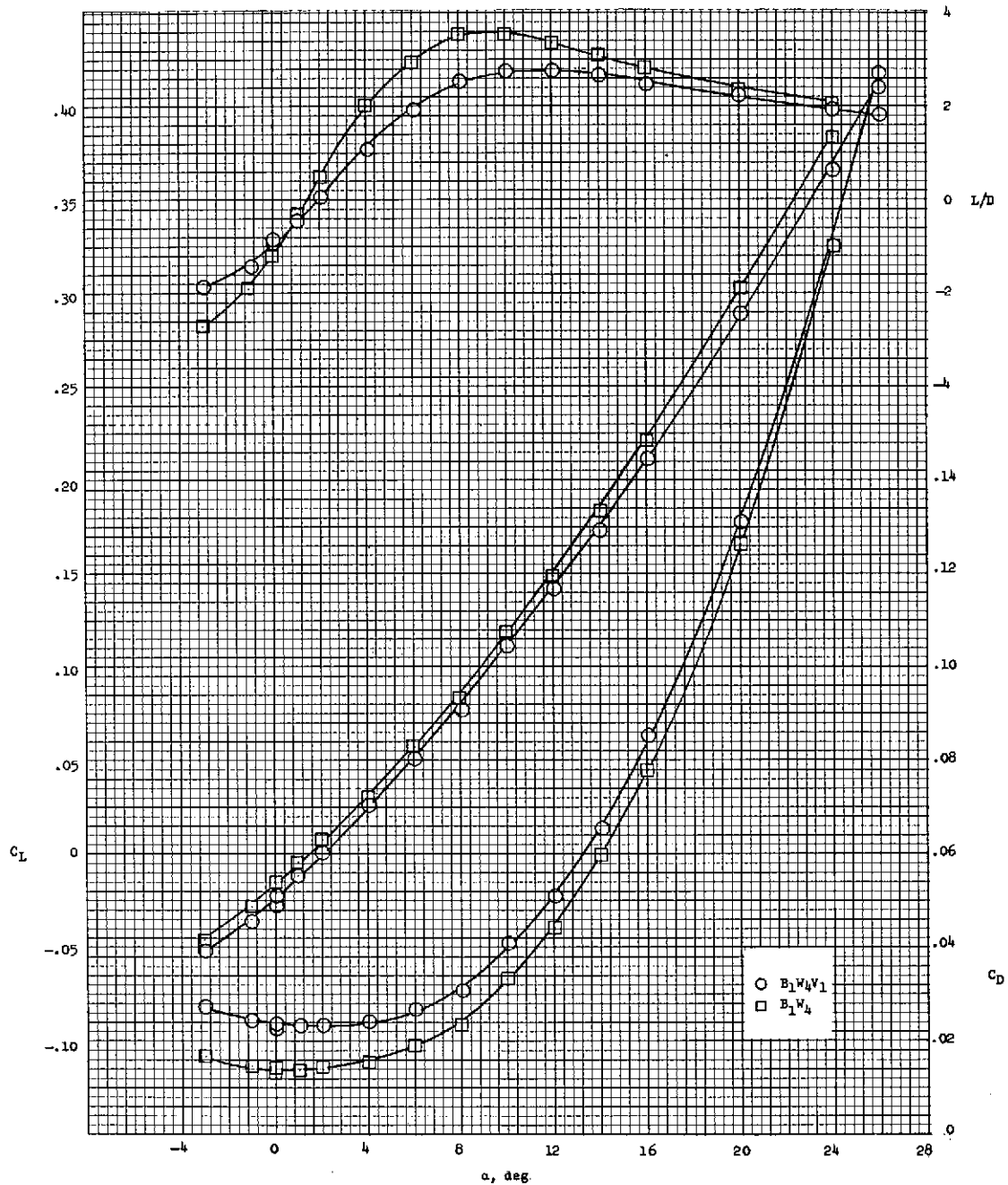
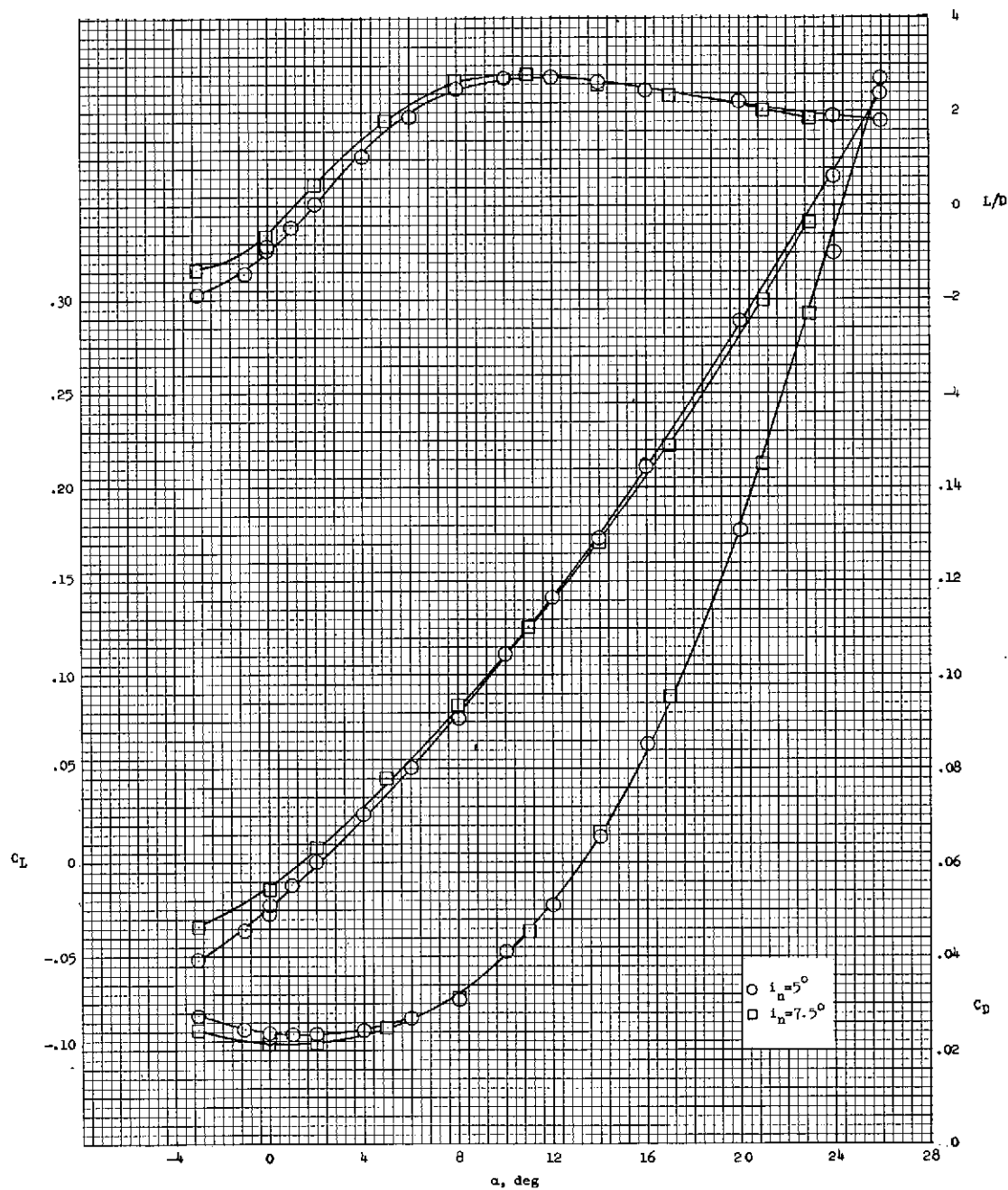


Figure 10.- Maximum lift-drag ratio plotted against Mach number.



(a) Effects of vertical fin.

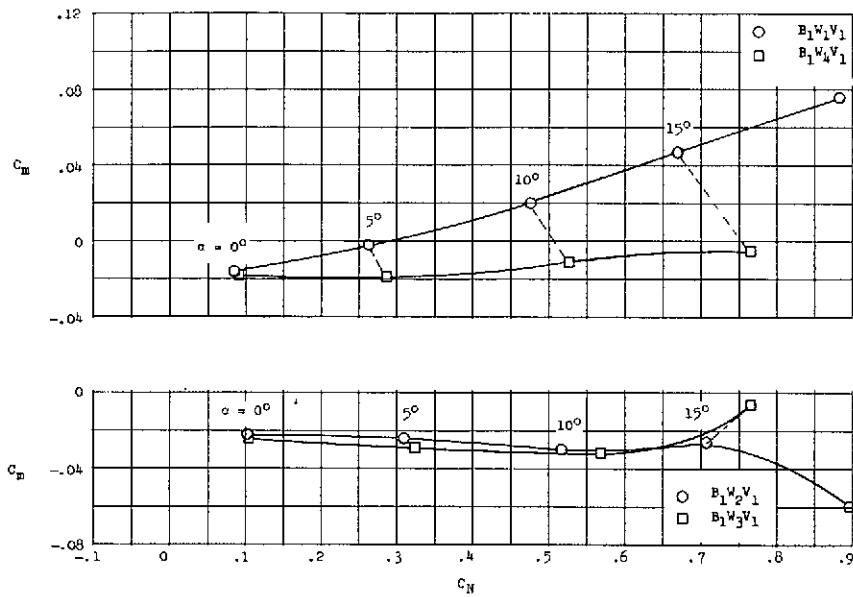
Figure 11.- Effects of vertical fin and nose incidence on longitudinal characteristics of  $B_1W_4$  models.  $M = 6.8$ ;  $R = 1.33 \times 10^6$ .



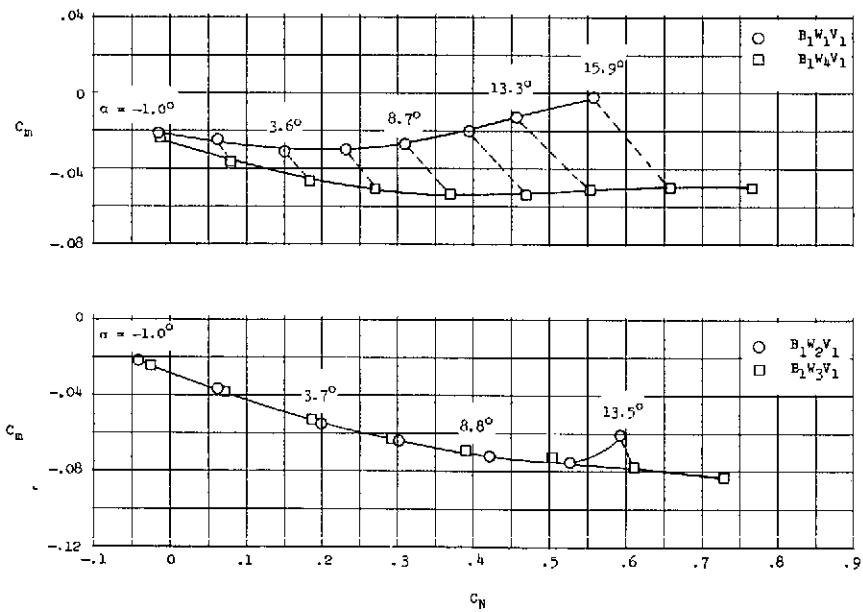
(b) Effects of nose incidence.

Figure 11.- Concluded.



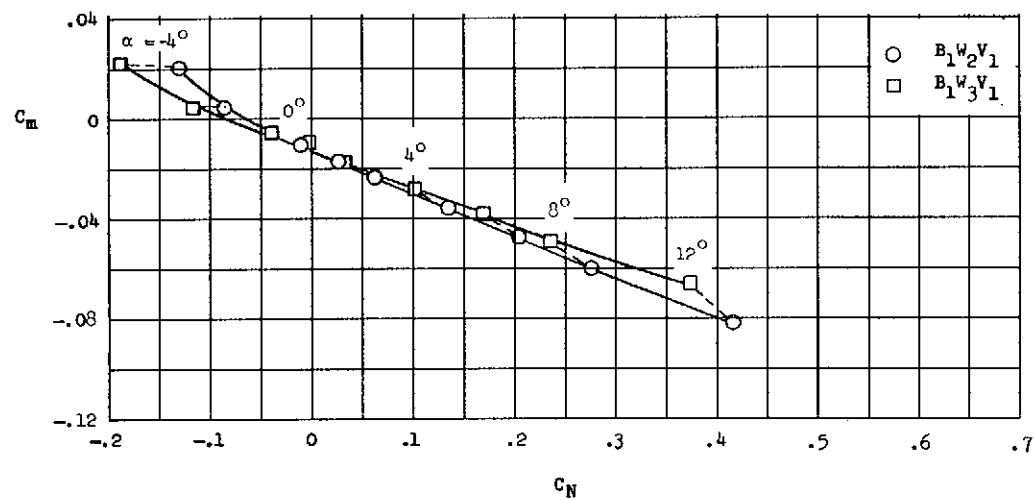
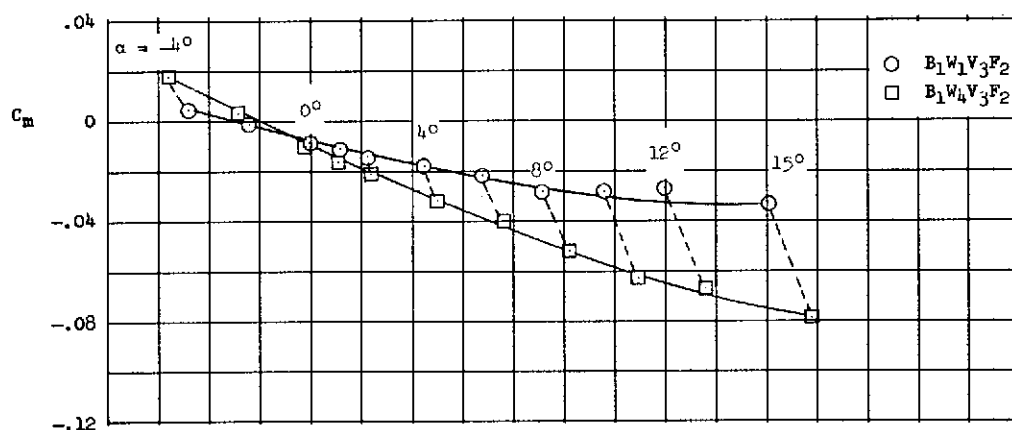
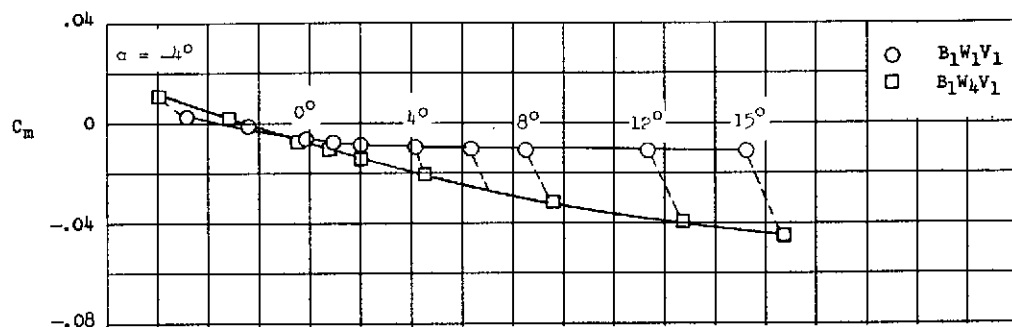


(a)  $M = 0.06; R = 1.5 \times 10^6$ .



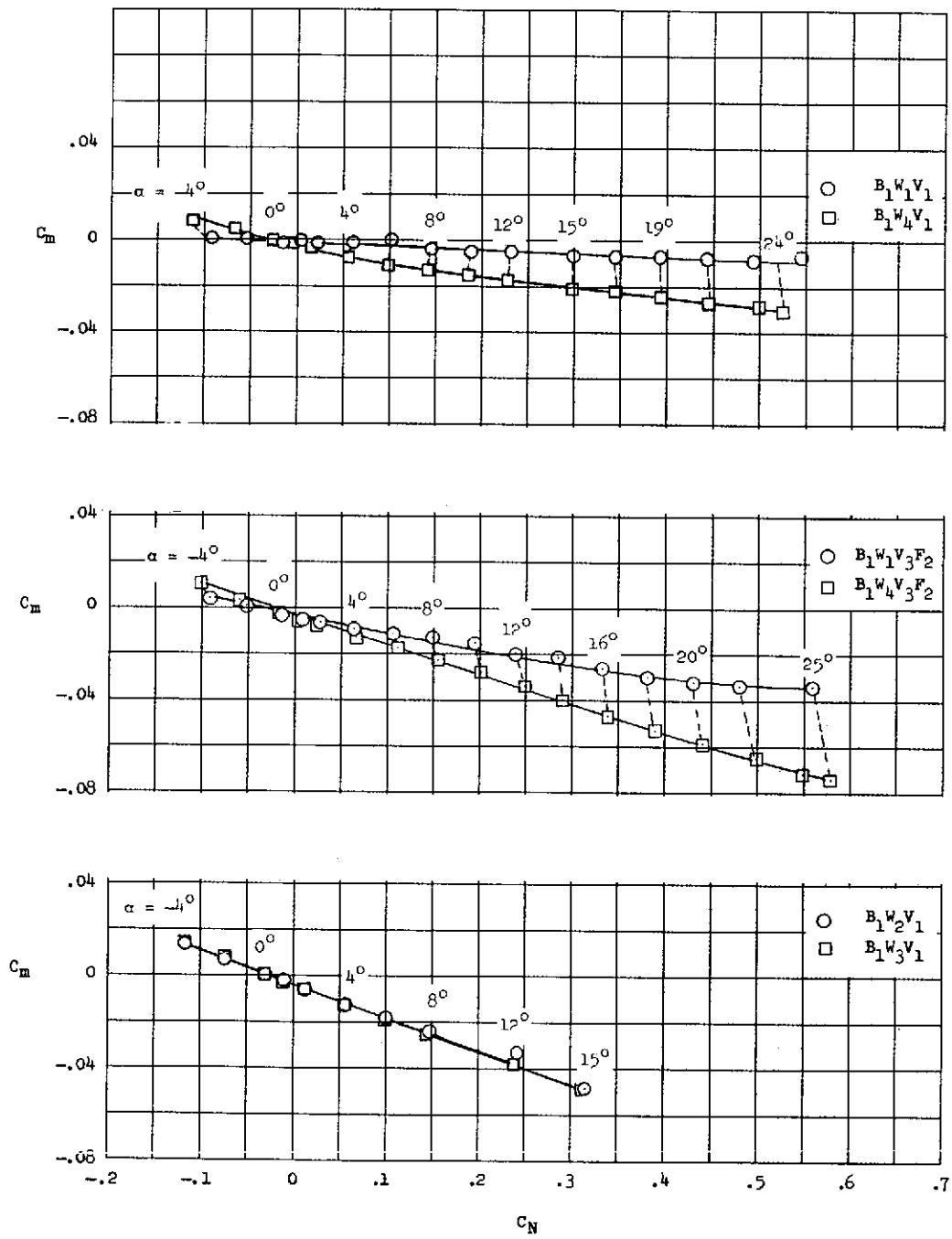
(b)  $M = 0.92; R = 4.1 \times 10^6$ .

Figure 12.- Pitching-moment coefficient plotted against normal-force coefficients for several Mach numbers.



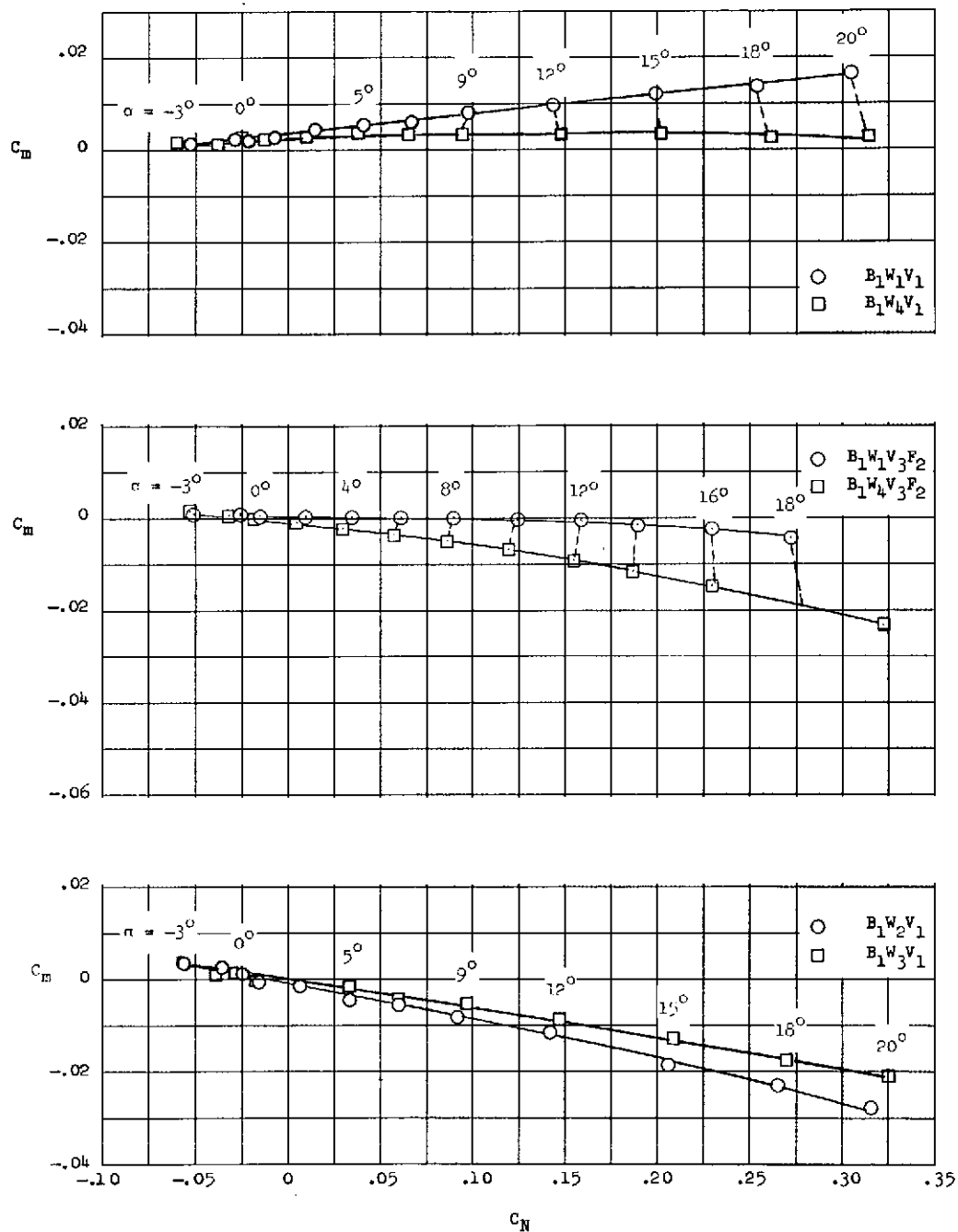
(c)  $M = 1.62$ ;  $R = 2.0 \times 10^6$ .

Figure 12.- Continued.



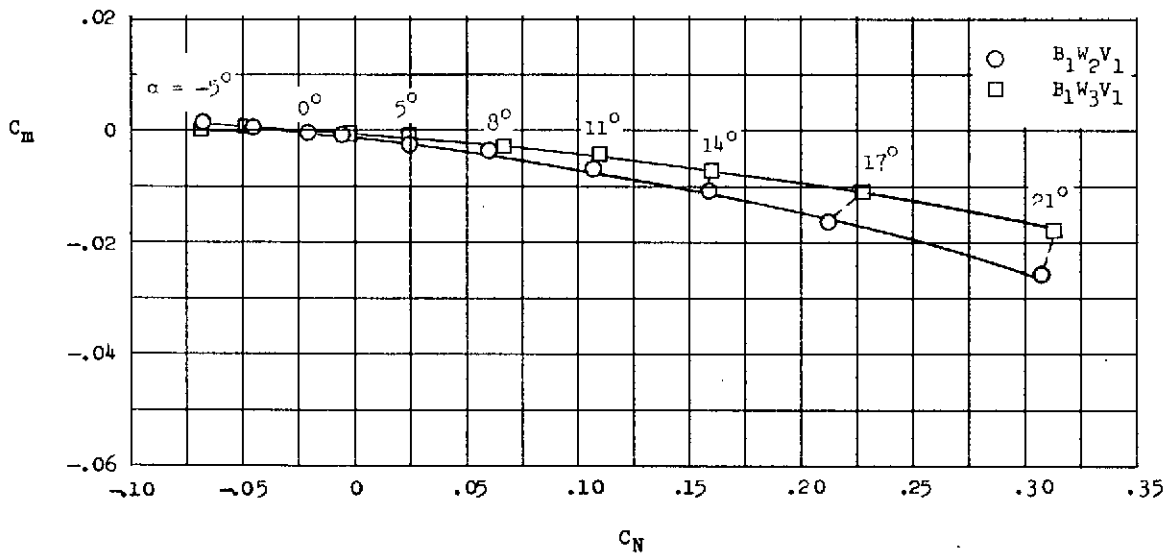
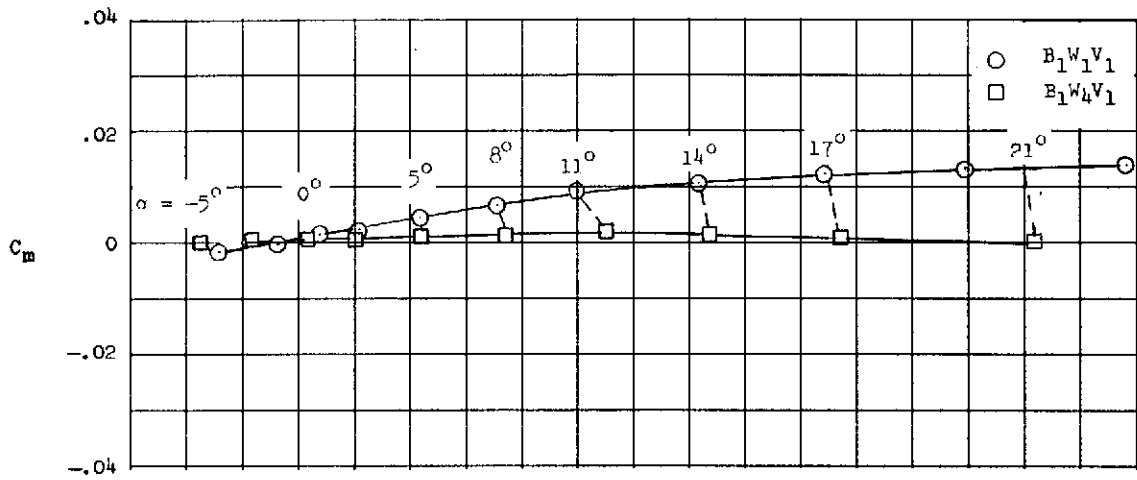
(d)  $M = 2.91$ ;  $R = 2.0 \times 10^6$ .

Figure 12.- Continued.



(e)  $M = 6.8$ ;  $R = 2.0 \times 10^6$ .

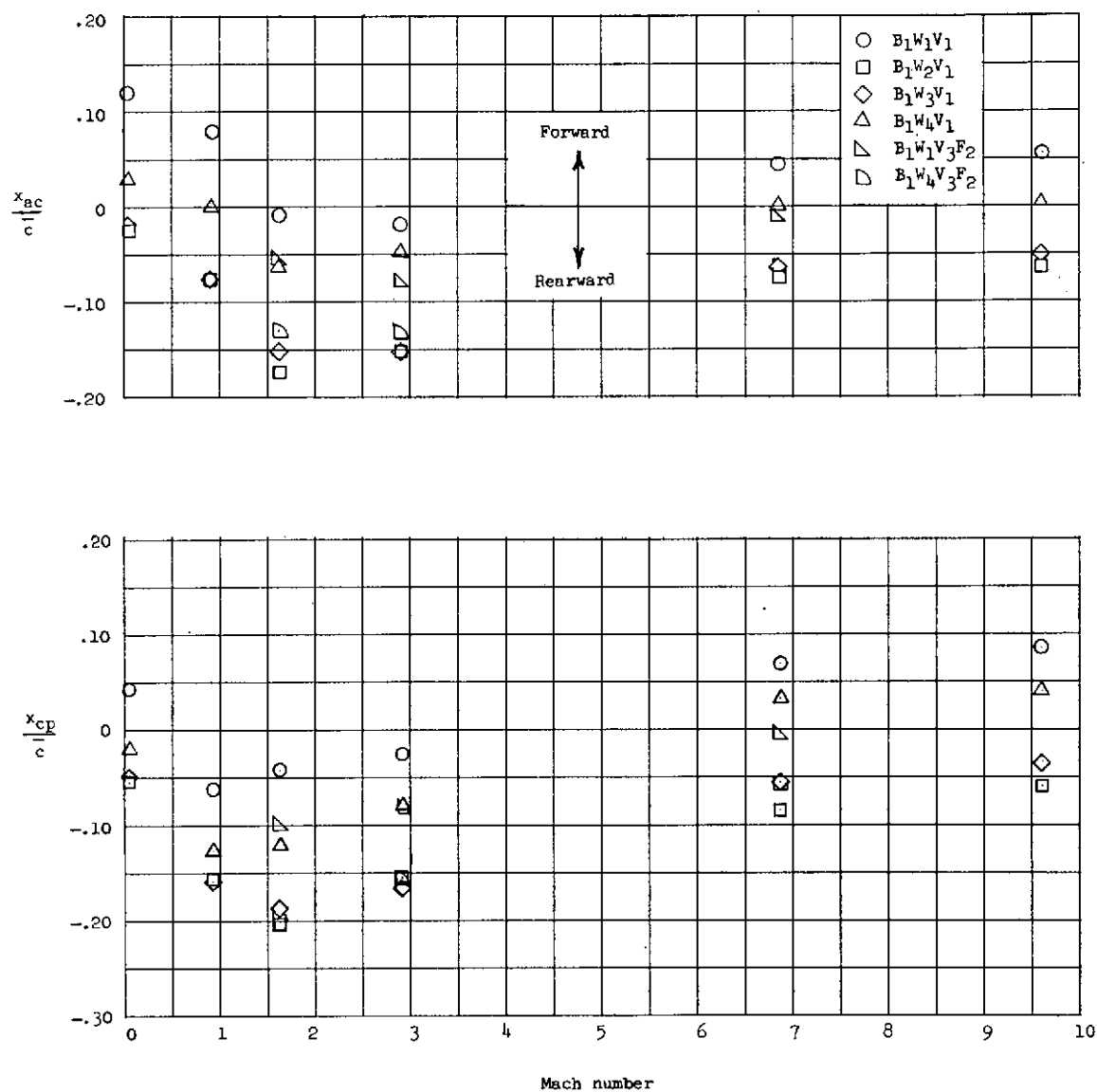
Figure 12.- Continued.



(f)  $M = 9.6$ ;  $R = 0.6 \times 10^6$ .

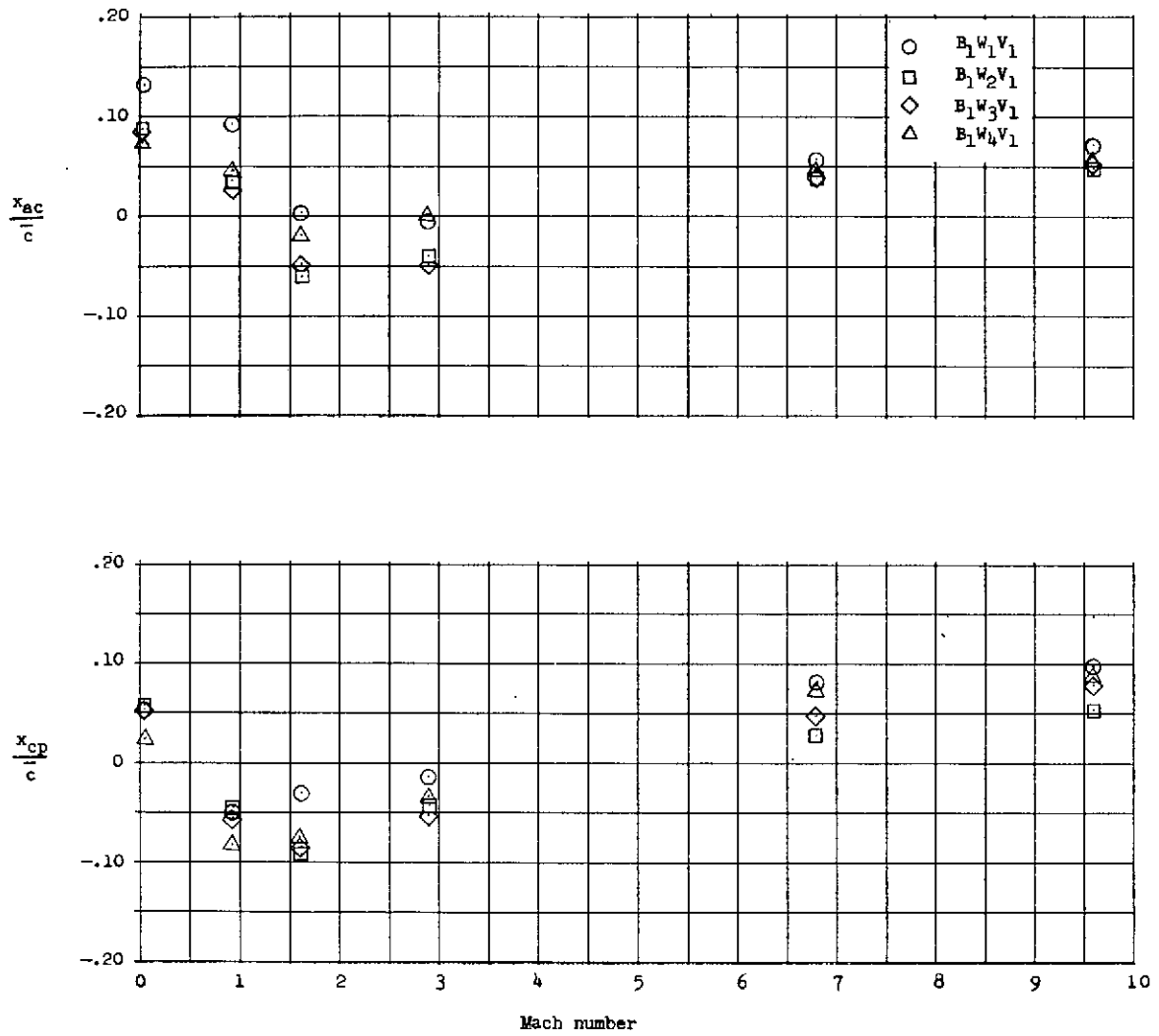
Figure 12.- Concluded.





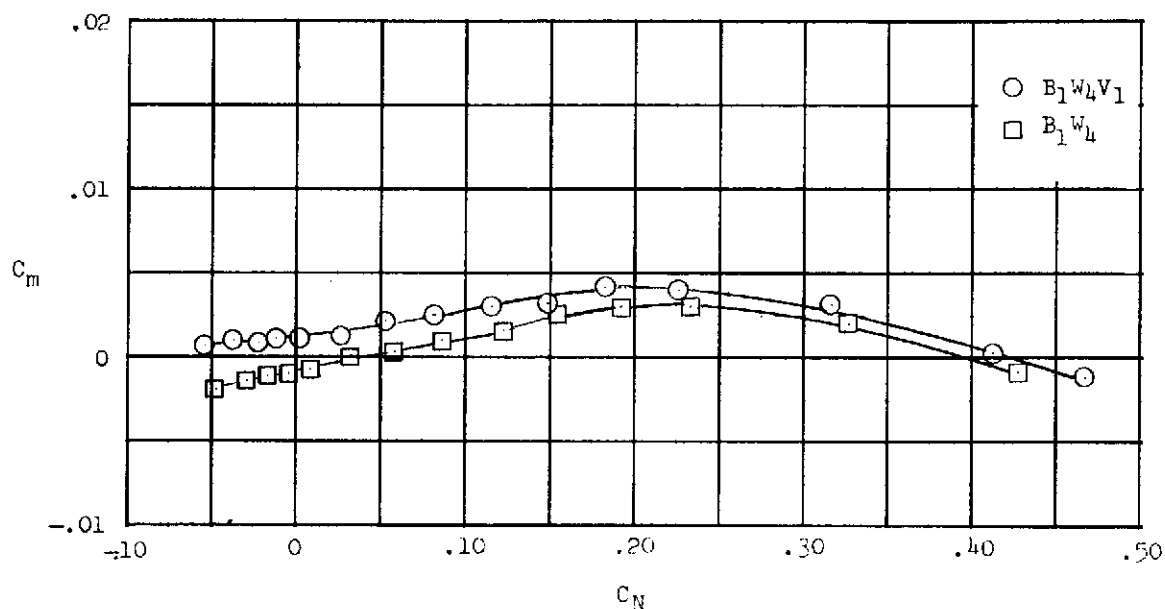
(a) Center of gravity at 0.641.

Figure 13.- Variation in aerodynamic-center and center-of-pressure locations with Mach number.  $\alpha = 10^\circ$ .



(b) Center of gravity at centroid of area.

Figure 13.- Concluded.



(a) Effects of vertical fin.

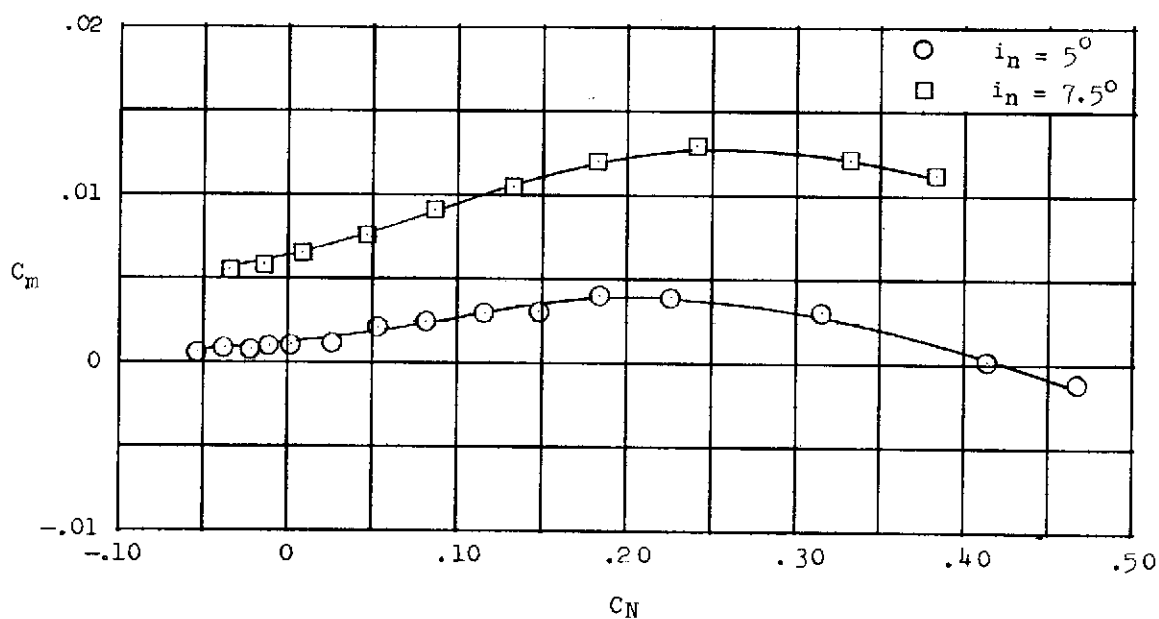
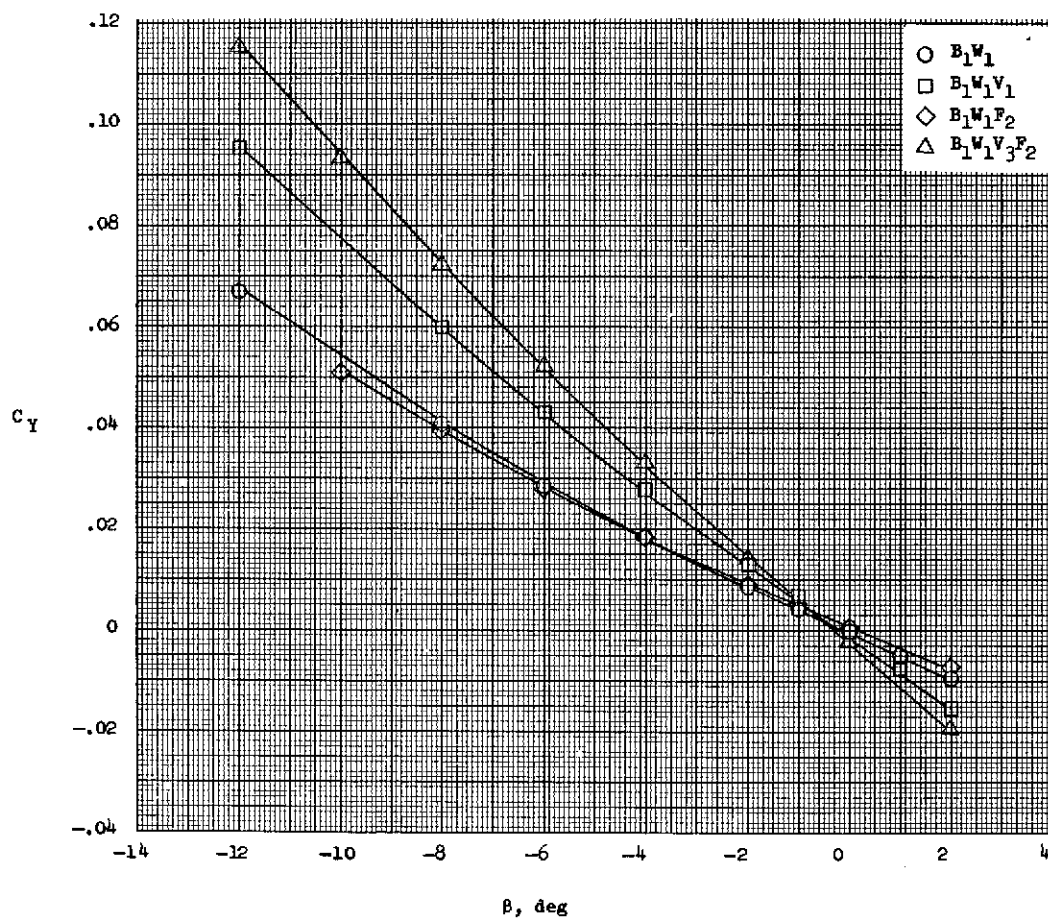
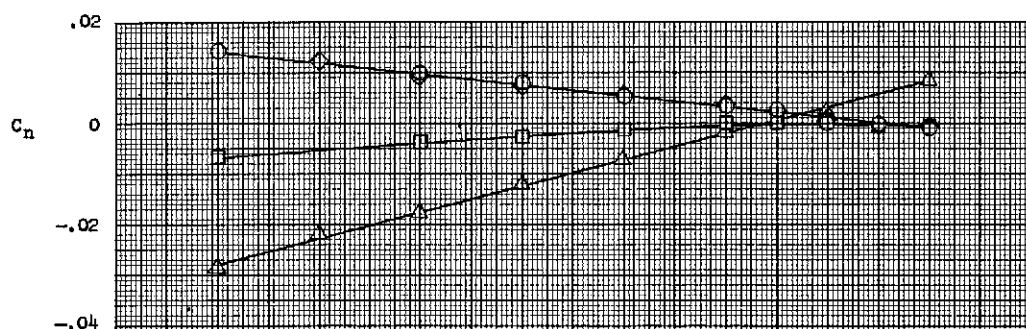
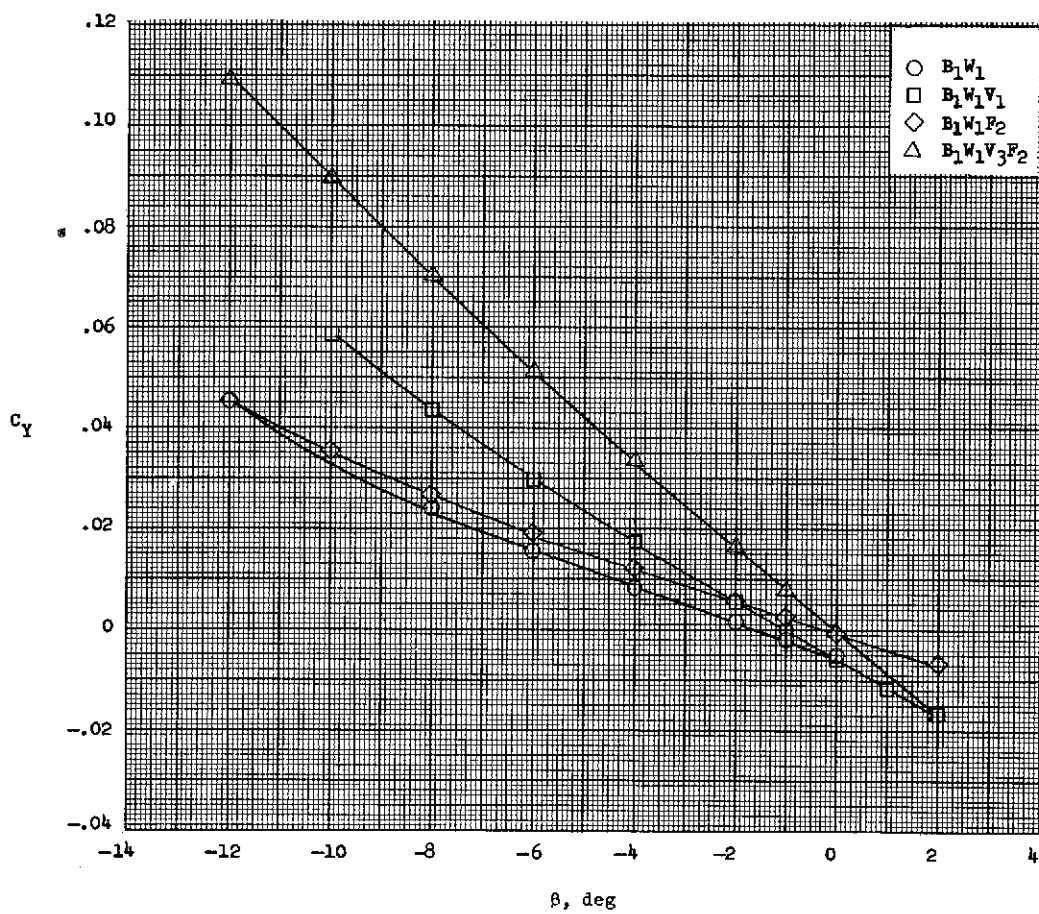
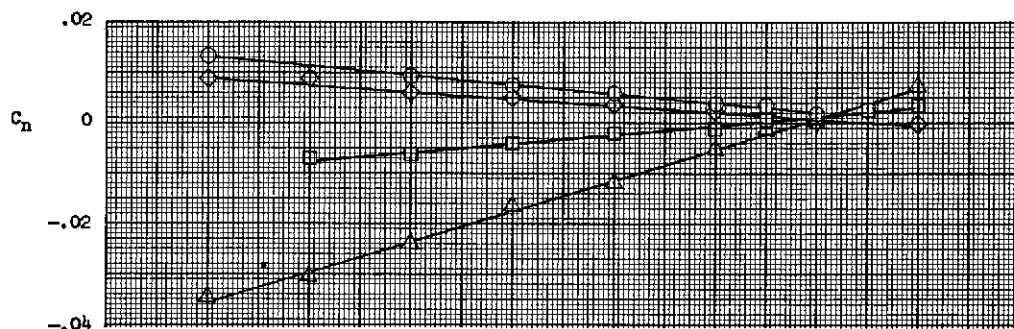
(b) Effects of nose incidence,  $i_n$ .

Figure 14.- Effects of vertical fin and nose incidence on pitching-moment coefficient for  $B_1W_4$  models.  $M = 6.8$ ;  $R = 1.33 \times 10^6$ .



(a)  $\alpha = 0^\circ$ .

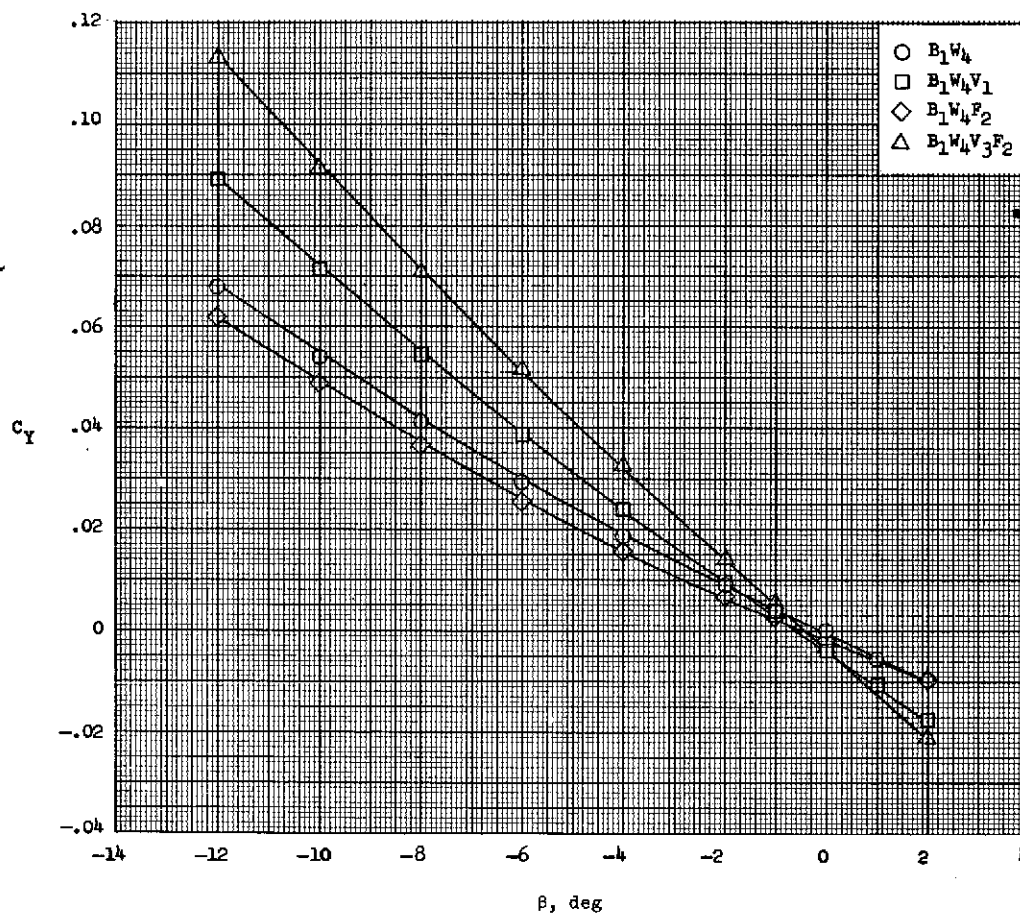
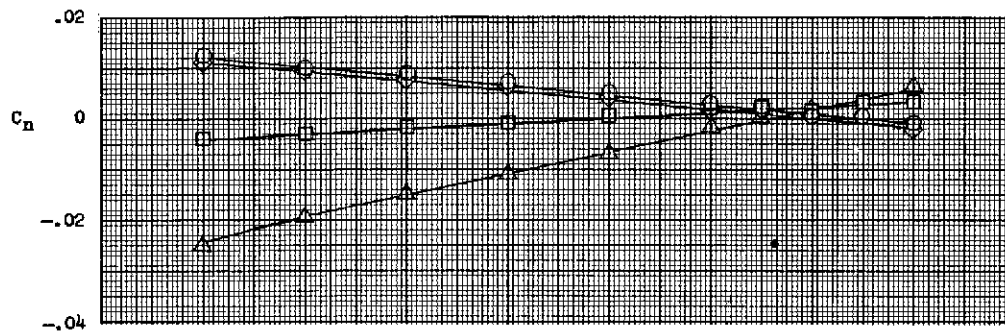
Figure 15.- Directional characteristics of  $B_1W_1$  models at  $M = 2.91$ .  
 $R = 2.0 \times 10^6$ .



(b)  $\alpha = 10^\circ$ .

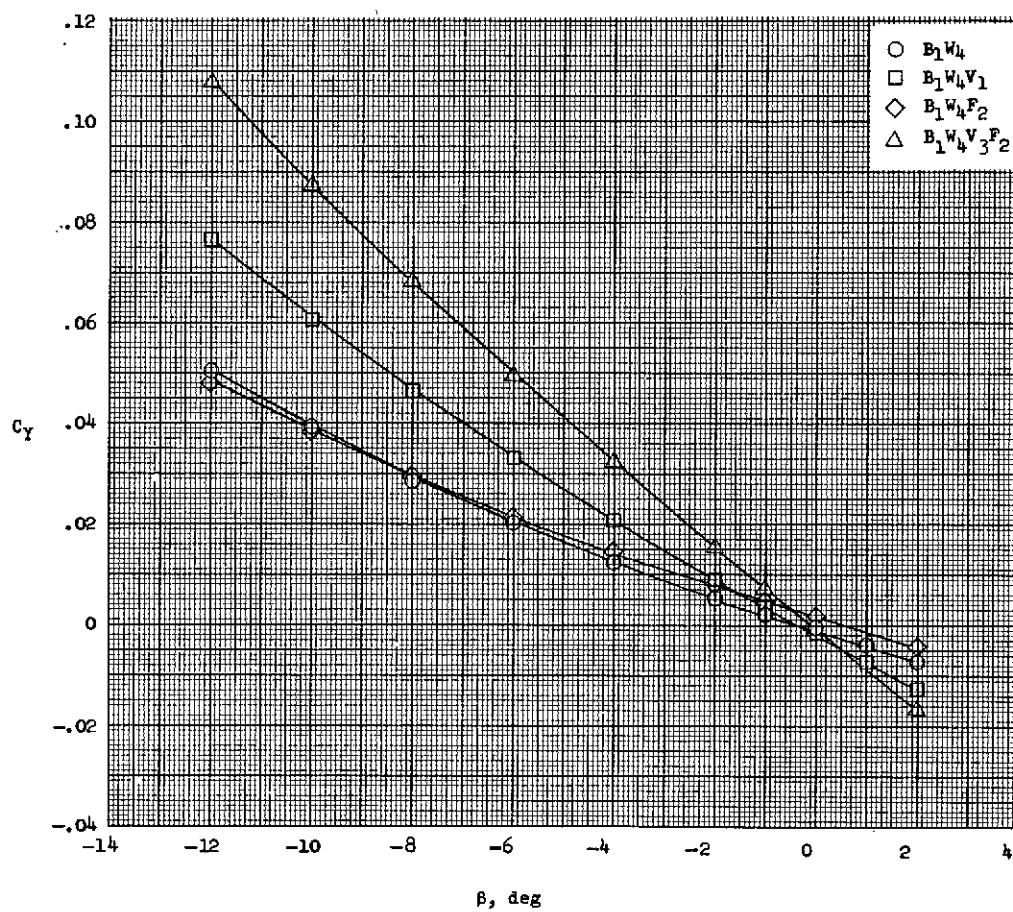
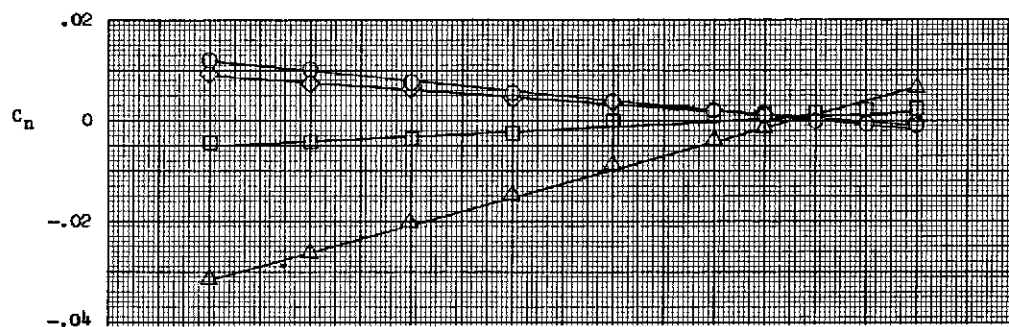
Figure 15.- Concluded.





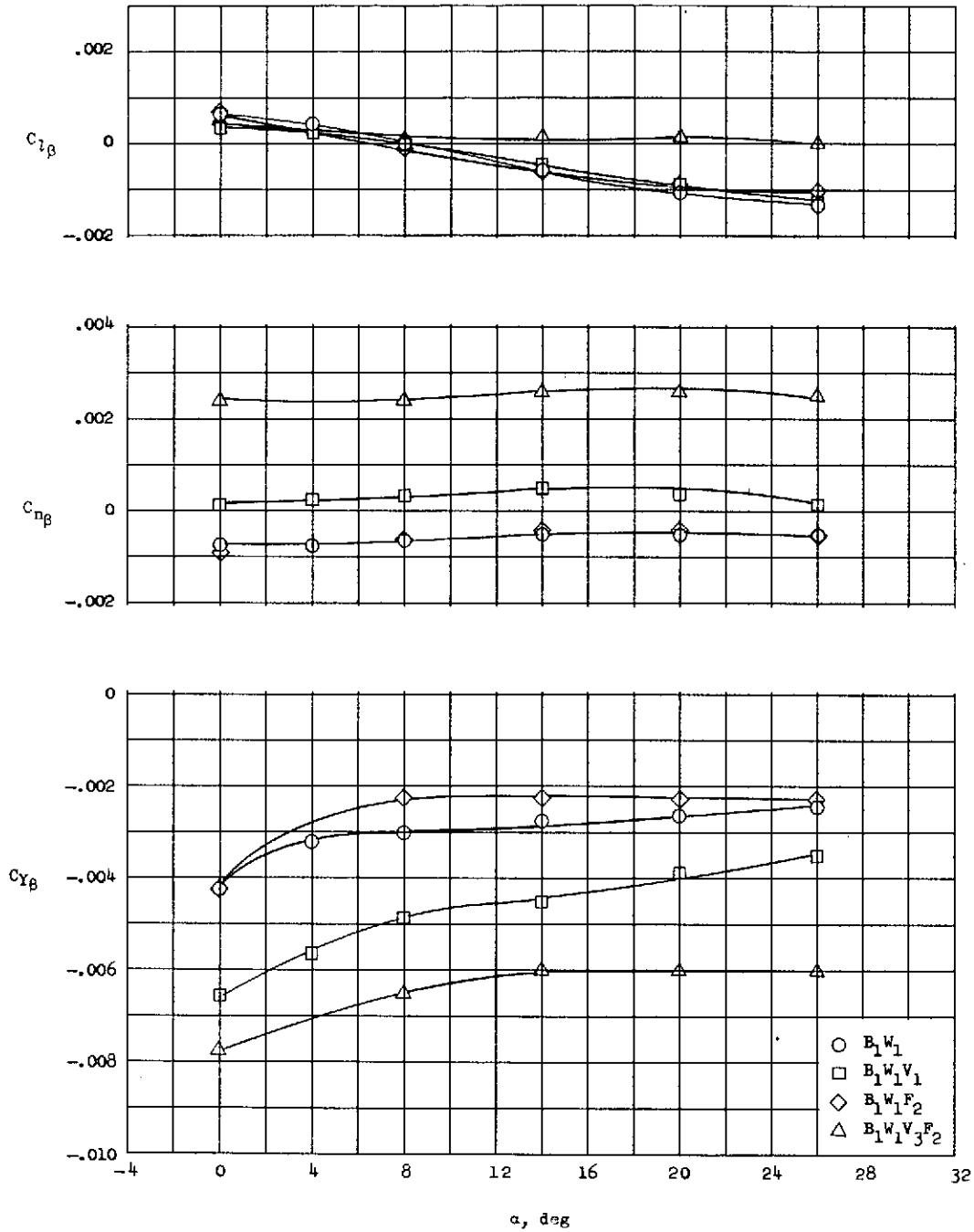
(a)  $\alpha = 0^\circ$ .

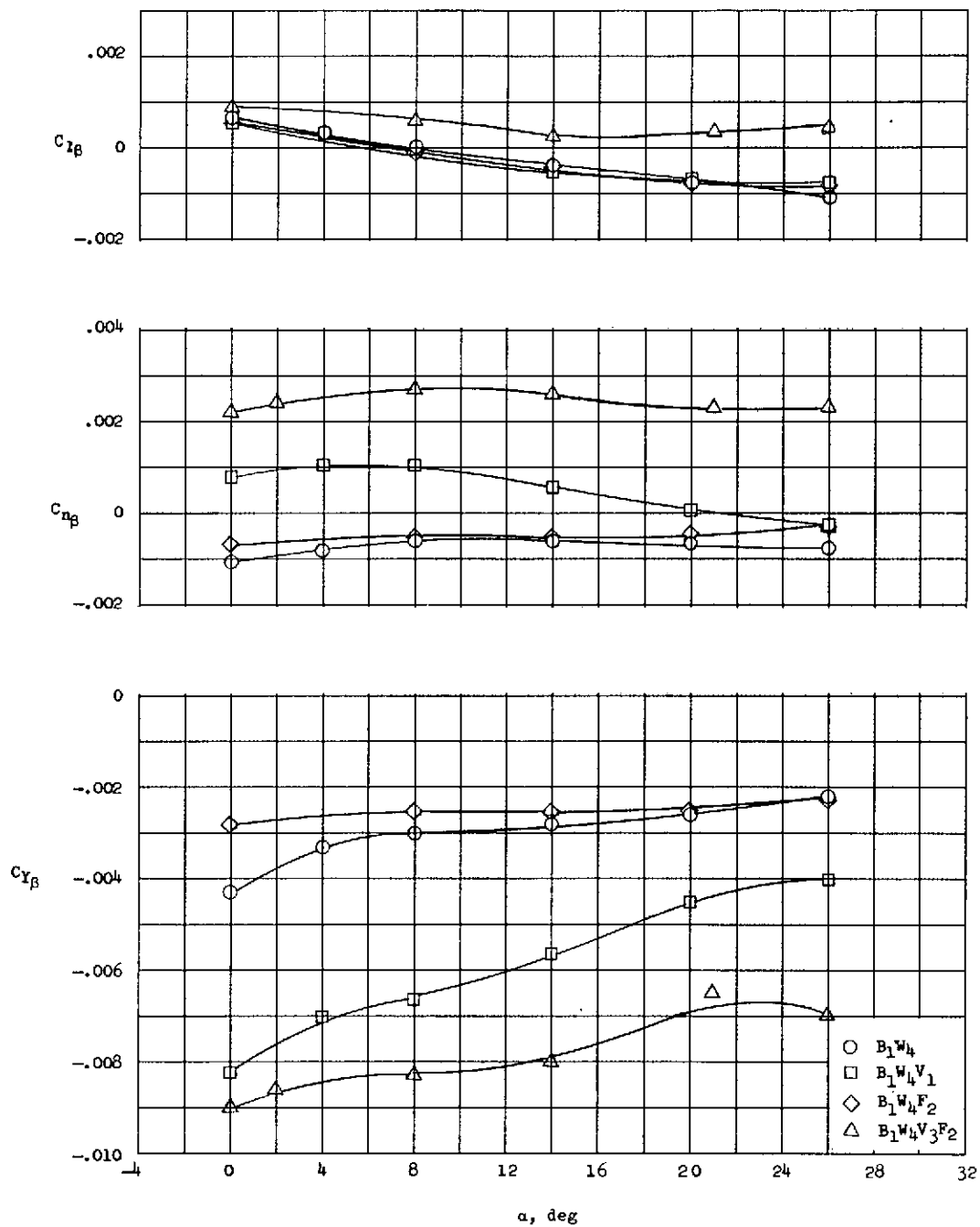
Figure 16.- Directional characteristics of  $B_1W_4$  models at  $M = 2.91$ .

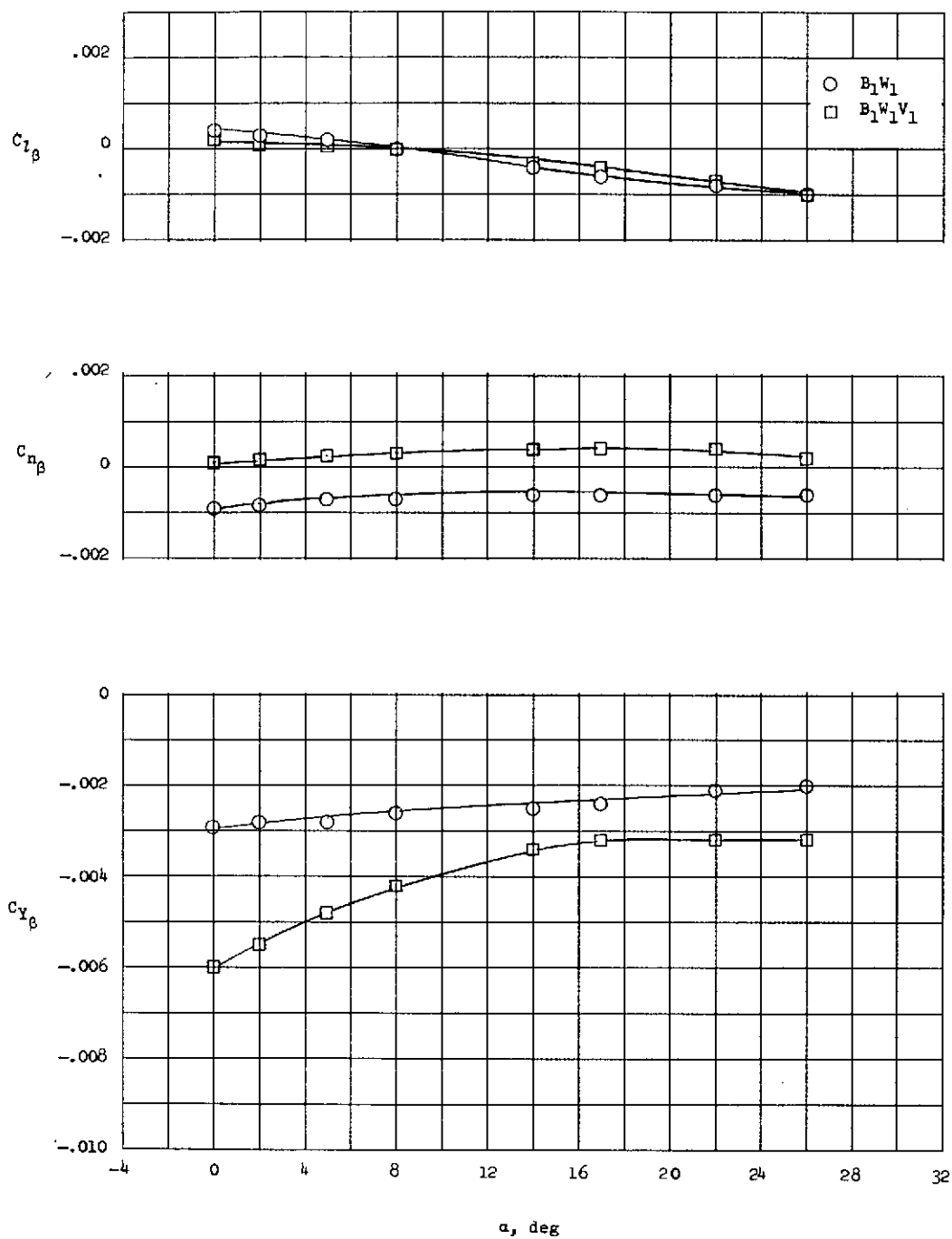


(b)  $\alpha = 10^\circ$ .

Figure 16.- Concluded.

(a)  $B_1W_1$  models.Figure 17.- Directional and lateral characteristics of configurations at  $M = 6.8$ ;  $R = 1.33 \times 10^6$ .



(a)  $B_1W_1$  models.Figure 18.- Directional and lateral characteristics of configurations at  $M = 9.6$ ;  $R = 0.6 \times 10^6$ .

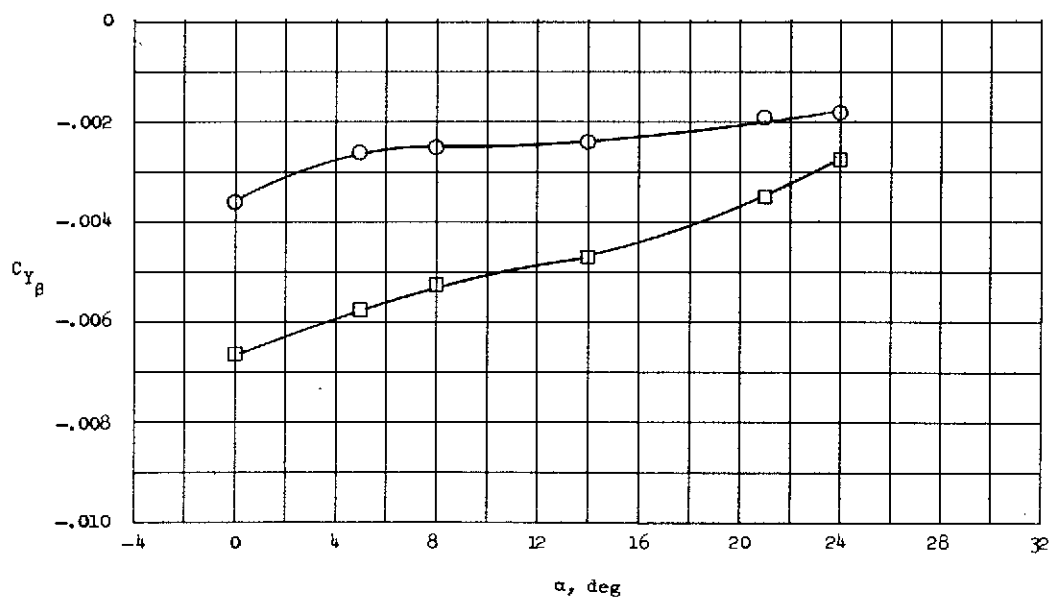
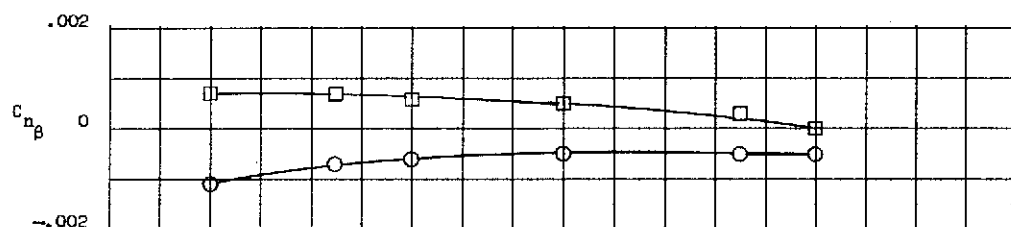
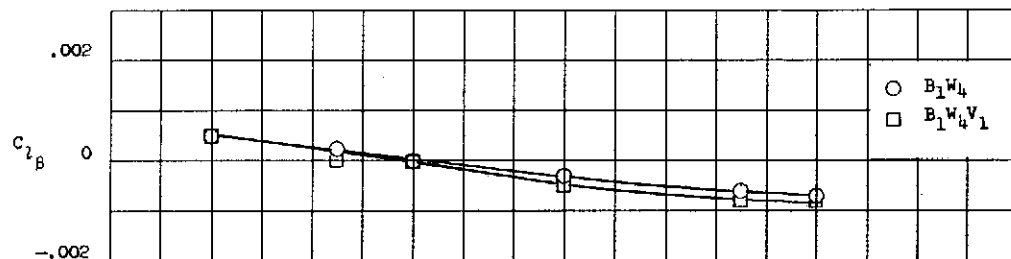
(b)  $B_1W_4$  models.

Figure 18.- Concluded.



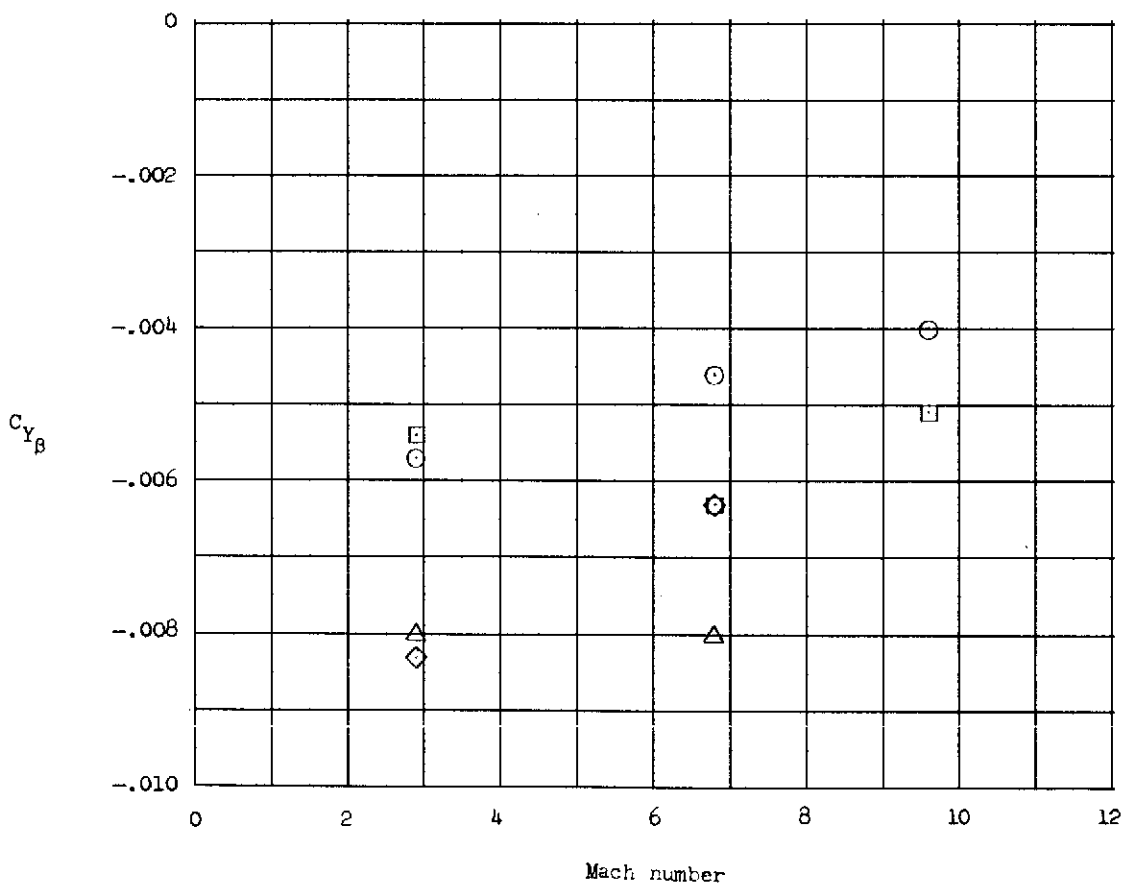
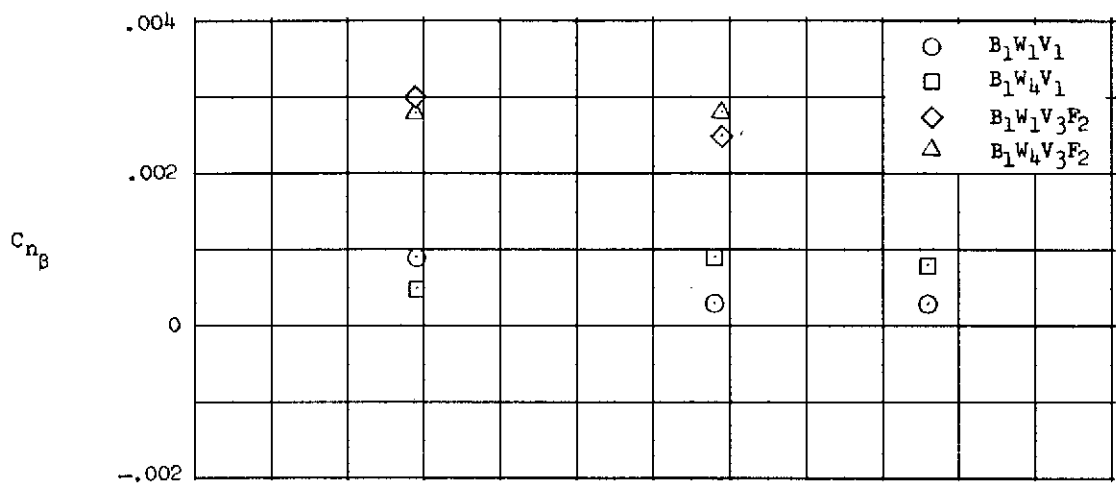


Figure 19.- Mach number effects on directional stability.  $\alpha = 10^\circ$ .

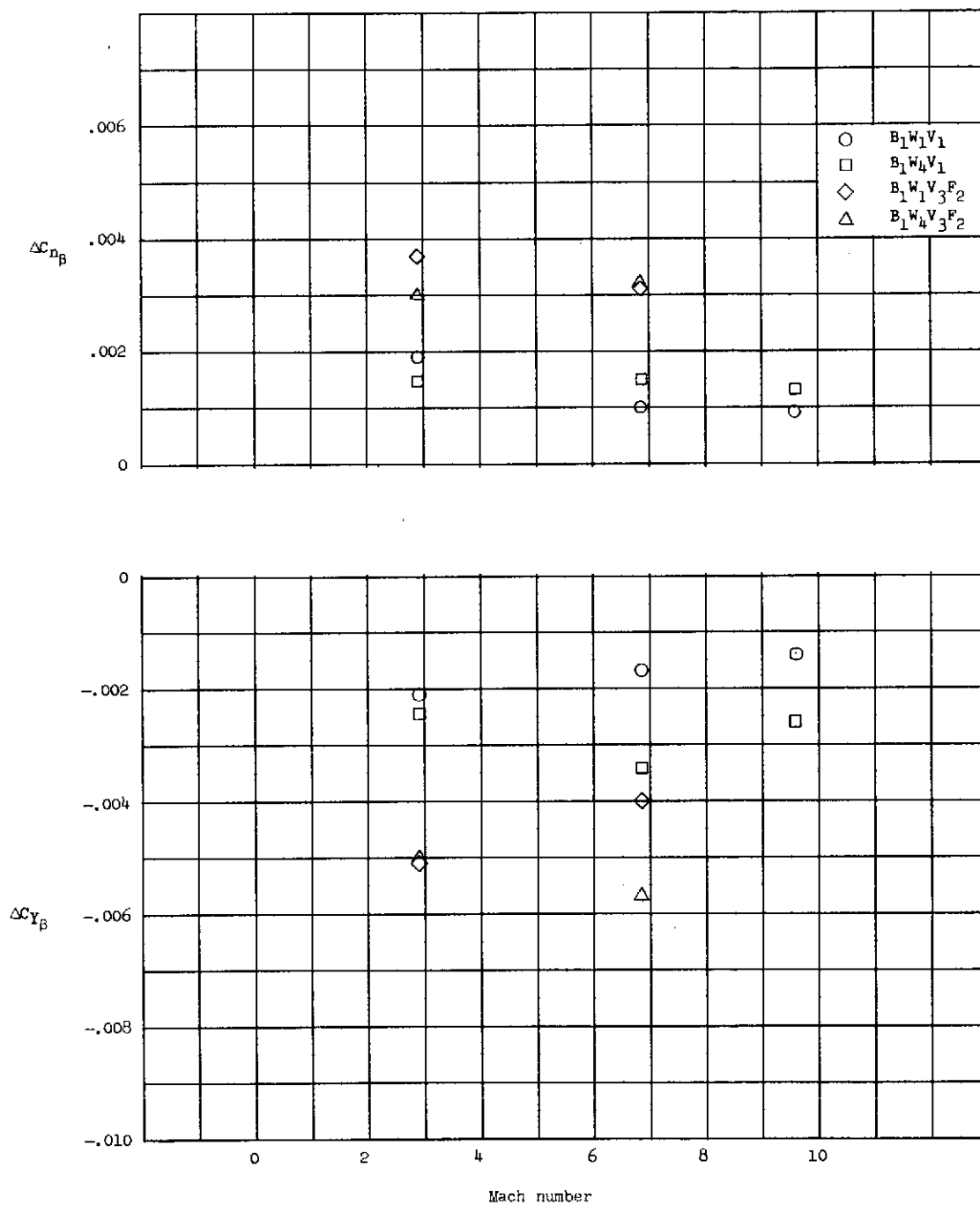


Figure 20.- Mach number effects on incremental directional stability due to adding tip fins.  $\alpha = 10^\circ$ .

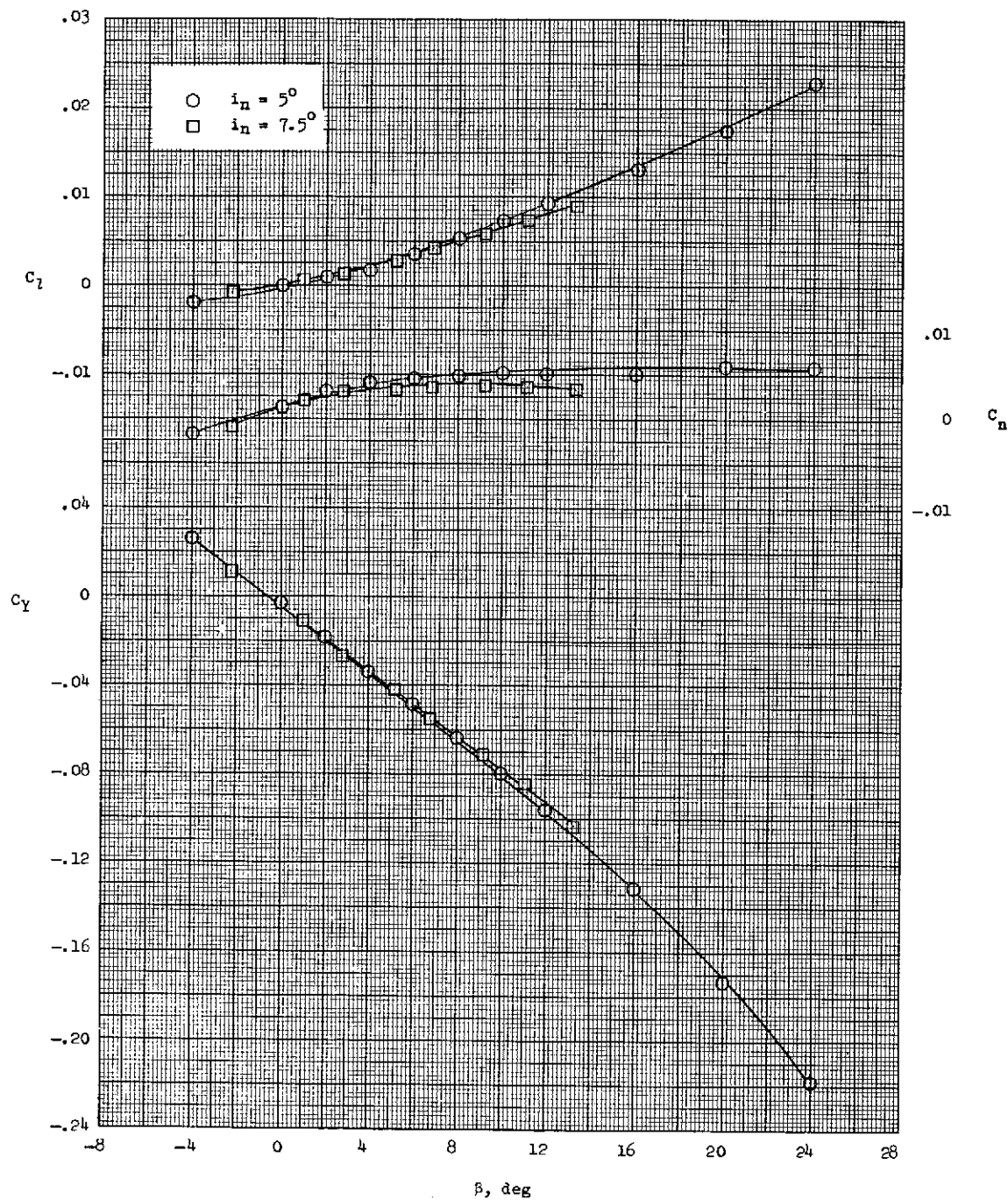


Figure 21.- Effects of nose incidence on directional and lateral characteristics of model  $B_1W_4V_1$  at  $M = 6.8$ .  $\alpha = 0^\circ$ .

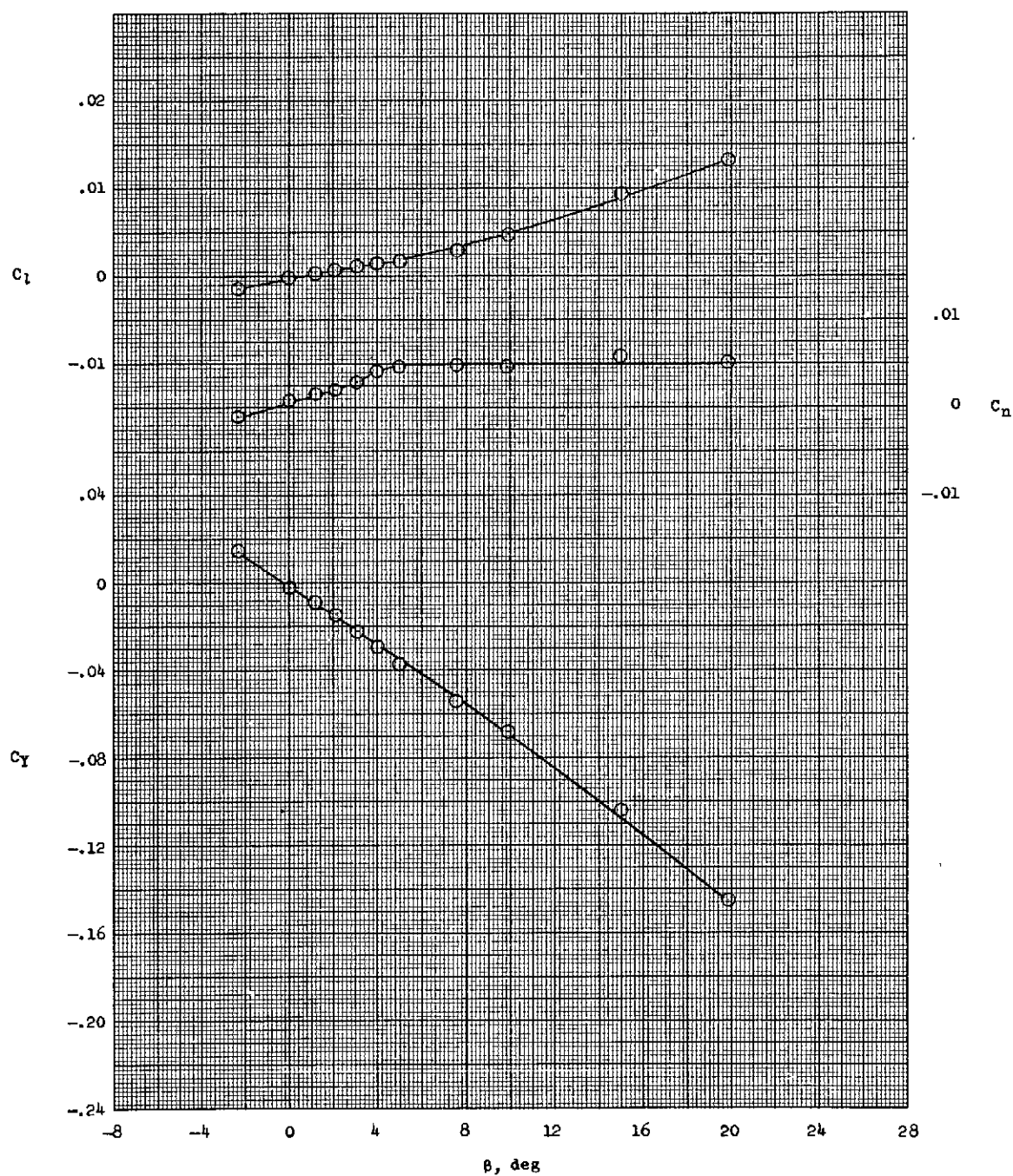


Figure 22.- Directional and lateral characteristics of model  $B_1W_4V_1$  at  $M = 9.6$ .  $\alpha = 0^\circ$ ;  $i_n = 5^\circ$ ;  $R = 1.33 \times 10^6$ .